

JGR Solid Earth

RESEARCH ARTICLE

10.1029/2024JB028898

Key Points:

- For la Réunion Island, GNSS-based tropospheric corrections outperform both weather-based corrections (ERA5 and GACOS)
- For Merapi volcano, the performance of GNSS-based corrections is similar to ERA5 with only 5 local stations
- The use of GNSS-based corrections paves the way for automated, real-time InSAR processing over tropical volcanoes

Supporting Information:

Supporting Information may be found in the online version of this article.

Correspondence to:

F. Albino,
fabien.albino@univ-grenoble-alpes.fr

Citation:

Albino, F., Gremion, S., Pinel, V., Bouygues, P., Peltier, A., Beauducel, F., et al. (2025). Benefits of GNSS local observations compared to global weather-based models for InSAR tropospheric corrections over tropical volcanoes: Case studies of Piton de la Fournaise and Merapi. *Journal of Geophysical Research: Solid Earth*, 130, e2024JB028898. <https://doi.org/10.1029/2024JB028898>

Received 26 FEB 2024

Accepted 19 MAR 2025





Author Contributions:

Conceptualization: F. Albino
Data curation: F. Albino, A. Peltier, F. Beauducel, Agus Budi Santoso
Formal analysis: S. Gremion, P. Bouygues
Funding acquisition: F. Albino
Investigation: S. Gremion, V. Pinel
Methodology: F. Albino
Project administration: F. Albino
Software: P. Bouygues
Supervision: F. Albino, V. Pinel
Validation: F. Albino

© 2025. The Author(s).

This is an open access article under the terms of the [Creative Commons Attribution-NonCommercial-NoDerivs License](#), which permits use and distribution in any medium, provided the original work is properly cited, the use is non-commercial and no modifications or adaptations are made.

Benefits of GNSS Local Observations Compared to Global Weather-Based Models for InSAR Tropospheric Corrections Over Tropical Volcanoes: Case Studies of Piton De La Fournaise and Merapi

F. Albino¹ , S. Gremion¹, V. Pinel¹ , P. Bouygues¹, A. Peltier^{2,3} , F. Beauducel² , J.-L. Froger⁴ , and Agus Budi Santoso⁵

¹Institut des Sciences de la Terre, Université Grenoble Alpes, Université Savoie Mont Blanc, CNRS, IRD, University Gustave Eiffel, Gières, France, ²Institut de Physique du Globe de Paris, Université Paris Cité, CNRS, Paris, France, ³Observatoire Volcanologique du Piton de la Fournaise, Institut de Physique du Globe de Paris, Université de La Réunion, La Réunion, France, ⁴Laboratoire de Géologie de Lyon: Terre, Planètes, Environnement, Université Jean Monnet - Faculté des Sciences et Techniques, Saint-Etienne, France, ⁵Center for Volcanology and Geological Hazard Mitigation (CVGHM), Yogyakarta, Indonesia

Abstract From repeat-pass interferometry, tropospheric signals often prevent the detection of ground deformation signals. In recent years, tropospheric corrections derived from global weather-based models have been implemented in several InSAR processing chains. In this study, we evaluate the performance of two weather-based models (ERA5 and GACOS) on two tropical volcanoes: Piton de la Fournaise and Merapi. For Piton de la Fournaise, the reduction of the tropospheric noise is efficient for ~30% and ~60% of the data sets for GACOS and ERA5, respectively. For Merapi, the performance reaches ~40% for GACOS and ~50% for ERA5. Although GNSS local stations provide real-time information about tropospheric delays, their potential for improving InSAR corrections on active volcanoes is under-exploited. Here, we produce local GNSS-based tropospheric corrections and compare their performance to global weather-based models. For Piton de la Fournaise, the gain of performance with ~34 GNSS stations is about 25% compared to ERA5 models. GNSS-based corrections increase the signal-to-noise ratio in InSAR time series allowing the detection of ground displacements between July and December 2021. For Merapi, GNSS-based models with only 5 stations spatially distributed at different elevations are as efficient as ERA5 models. GNSS-based corrections induce a decrease in the noise level from values > 1–0.5 cm in a period of quiescence. Here, we show that GNSS-based models are an efficient alternative to global weather-based models for instrumented volcanoes. The proposed approach paves the way toward near real-time InSAR monitoring of volcanic unrest and other processes (landslides, groundwater extraction).

Plain Language Summary In tropical regions, the use of differential radar interferometry to detect ground displacements is challenging due to the presence of atmospheric interference. Strategies to mitigate these atmospheric artifacts are required. Here, we test the performance of common weather-based models, ERA5 and GACOS, on two active volcanoes Piton de la Fournaise and Merapi. Our findings show that the performance of these models is limited as they usually reduce the atmospheric noise for less than half of the data sets. We explore data collected from Global Navigation Satellite System (GNSS) stations to improve the performance. Although GNSS stations are primarily installed for the monitoring of volcanic ground deformation, they can provide valuable information about atmospheric conditions, yet these data are underutilized. To fill this gap, we develop a workflow to produce GNSS-based atmospheric corrections. For Piton de la Fournaise, GNSS-based models largely outperform the performance obtained with weather-based models. For Merapi, only five stations are required for GNSS-based models to perform as well as ERA5 models. As GNSS-based models can be obtained in near real-time, our approach paves the way for the implementation of routine InSAR monitoring of ground displacements in Volcano Observatories.

1. Introduction

Differential synthetic aperture radar interferometry technique (DInSAR) enables the production of interferograms that correspond to the map of the total phase delays, corrected from topographic effects using a DEM, between

Writing – original draft: F. Albino,
S. Gremion
Writing – review & editing: F. Albino,
S. Gremion, V. Pinel, A. Peltier,
F. Beauducel, J.-L. Froger

two SAR images acquired at different times along the same orbit (Hanssen, 2001). Since the 1990s, DInSAR has been used to measure surface displacements of a few centimeters associated with different geological events such as earthquakes, volcanic eruptions, and landslides (Massonnet et al., 1993; Rosen et al., 1996; Rott & Nagler, 2006). On active volcanoes, ground deformation signals may be observed before, during and after an eruption and they are caused by several processes: reservoir pressurization, magma/fluid migration, lava flow compaction, flank sliding (Biggs & Pritchard, 2017; Pinel et al., 2014; Sparks et al., 2012). The detection of such signals with DInSAR can be limited by several factors: high gradients of topography causing localized loss of information, temporal decorrelation of the signals on vegetated areas and presence of atmospheric artifacts (Ebmeier et al., 2013). Indeed, the phase delay between the satellite and the ground is affected by the refraction of the electromagnetic wave during its propagation into the atmosphere (de Munck & Spoelstra, 1992; Zebker et al., 1997). For SAR interferometry, atmospheric artifacts are caused by phase delays occurring in the troposphere (between 0 to 7–20 km). In addition, phase delays in the ionosphere (between 60 and 1,000 km) can induce long wavelength signals, especially in L-band interferograms over tropical regions (Meyer, 2010).

Tropospheric delays can be separated into a hydrostatic component of a few meters and a wet component of only a few centimeters (de Munck & Spoelstra, 1992). GNSS measurements can provide the temporal evolution of tropospheric delays. Such procedure is well established and operational for many weather applications (Guerova et al., 2016). During the GNSS processing, the hydrostatic delays are derived through empirical models that depend on surface measurements (pressure and temperature) at the stations (Hopfield, 1971; Saastamoinen, 1973). Temporally, hydrostatic delays vary with diurnal cycles (0.2 mm to ~1 cm) and annual cycles (tens mm) (Jin et al., 2009). Wet delays are obtained by differentiating the measured total delays and the modeled hydrostatic delays. Values for wet delays mainly depend on the temperature and the water vapor content that quickly varies in time and space.

For DInSAR, each interferogram records the difference of the total tropospheric phase delays between two epochs. Although the hydrostatic component represents 80%–90% of the total tropospheric delay, the difference for a short-duration interferogram will be dominated by the wet component as the hydrostatic delay remains almost constant. The difference of tropospheric phase delays observed in interferograms is often decomposed into two components: a stratified part that correlates with the topography containing part of the hydrostatic and wet delays (as both depend on the tropospheric path length and consequently on the elevation), and a turbulent part that corresponds to the residual signals uncorrelated with the topography (Hanssen, 2001).

In tectonic and volcanic settings, numerous studies have developed and applied frameworks for mitigating tropospheric noise to improve the detection of ground deformation signals such as:

1. Stacking of N interferograms to reduce the variance of atmospheric noise (Biggs et al., 2007; Emardson et al., 2003; Wright et al., 2001).
2. Low-pass filtering on InSAR time series with the assumption that atmospheric noise is random in time and ground deformation is stationary during the averaging periods (Hooper et al., 2004; Schmidt & Bürgmann, 2003).
3. Empirical models derived from fitting with linear, exponential or power-law functions the relationship between the phase delays in the interferogram and the elevation; the correlation is estimated on all area (Cavalié et al., 2007; Elliott et al., 2008; Remy et al., 2003) or at multiple scales (Bekaert et al., 2015; Shirzaei & Bürgmann, 2012).
4. Models based on external data sets such as spectrometers (MODIS/MERIS) (Rémy et al., 2015) and global weather analysis (GACOS, ERA, WRF, NAAR) (Albino et al., 2020; Jung et al., 2013; Parker et al., 2015; Pinel et al., 2011; Stephens et al., 2020).
5. Zenith Tropospheric Delays (ZTD) derived from GNSS measurements (Onn & Zebker, 2006; Shamshiri et al., 2020; Yu, Li, & Penna, 2018).

The methods (1) and (2) have limited applications as they are only removing part of the tropospheric noise that is random in time. The method (3) only corrects the stratified component and the correlation phase-elevation must be derived on non-deformed areas to avoid correcting ground deformation signals. To overcome these issues, inversion strategies have been proposed to jointly evaluate the tropospheric stratified delays and persistent deformation signals in InSAR time series (Beauducel et al., 2000; Liang et al., 2018). The methods (4–5) have the advantage of providing corrections that are independent of the raw data (e.g., interferogram). Spectrometers have the best spatial resolution (~1 km); however, their application is largely limited on tropical volcanoes due to the

presence of clouds. The performance of the method (4) is usually poor at local scales as models have spatial resolution larger than 10 km. The method (5) requires a dense and well-distributed network of GNSS stations and for this reason, it has been mainly applied on well-instrumented regions such as Japan, southern California, UK and Norway (Shamshiri et al., 2020; Yu, Li, & Penna, 2018). However, many active volcanoes are instrumented at a local scale with GNSS networks operated by Volcano Observatories to monitor ground displacements. So far, such GNSS ZTD measurements have not been used for routinely mitigating tropospheric noise on active volcanoes. Therefore, the performance of such GNSS-based models should be compared to global weather-based models to evaluate the benefit of the approach for routine InSAR processing.

Since the launch in 2014 of the Sentinel-1 radar mission operated by the Copernicus program, many InSAR processing workflows have been designed to routinely produce ground displacement maps at regional or global scale (Costantini et al., 2021; Lazecký et al., 2020; Thollard et al., 2021). Most of the InSAR processing systems are using global weather models for several reasons.

1. It can easily be applied for each location on Earth compared to the empirical method
2. It does not require prior knowledge of the expected deformation or the tropospheric signals (e.g., fitting function, scale of correlation)
3. It corrects both the stratified and turbulent components at once

The commonly used strategy in the literature is to systematically apply corrections to all produced interferograms. This approach is effective at global and regional scales for mitigating large-wavelength atmospheric signals. However, previous studies looking at the performance of weather-based atmospheric corrections at the scale of volcanoes have shown several limitations. At the Agung volcano, GACOS weather-based models become effective only if the method is combined with empirical methods (e.g., removal of a ramp and phase-elevation correction) (Albino et al., 2020). For the Nicaraguan volcanoes, weather-based corrections show performance for less than half of the data sets, with a reduction of tropospheric noise for 48% (ERA5), 31% (GACOS) and 42% (NAAR) of the interferograms at the Telica volcano and for 43% (ERA5), 42% (GACOS) and 38% (NAAR) of the interferograms at the Masaya volcano (Stephens et al., 2020). Such studies highlighted that the method that provides the best performance is highly dependent on the test site and the combination of different approaches can improve corrections.

The ECMWF data sets have coarse resolution compared to interferograms: ERA5 (5th generation atmospheric reanalysis) products have a spatial resolution of ~30 km and a temporal resolution of 1 hr and the HRES (high-resolution) products have a spatial resolution of ~10 km and a temporal resolution of 6 hr. The poor performance of the weather-based atmospheric corrections on volcanoes can be the consequence of the coarse spatial/temporal resolution and the fact that ground measurements assimilated by such models are very sparse in the vicinity of volcanoes. In a volcanic environment, the atmospheric signals observed can be characterized by (a) short wavelength (<10 km) due to the difference of elevation between the base and the summit of the edifice and (b) short duration (<1 hr) due to disturbances originating from rapid changes in the atmospheric conditions. Such characteristics will be enhanced in cases of high-elevated stratovolcanoes or oceanic volcanic islands located in tropical climates.

In this paper, we will first carry out a statistical analysis of the performance of weather-based atmospheric corrections on two volcanic test sites: (a) Piton de la Fournaise and (b) Merapi. Piton de la Fournaise (2,632 a.s.l.) is an active shield volcano located in the south-east of La Réunion Island on the Indian Ocean. The island is often impacted by strong weather disturbances such as heavy rainfall and tropical cyclones. Merapi (2,910 m a.s.l. since the 2010 eruption) is an active stratovolcano located on Java island (Indonesia) at ~20 km north from the city of Yogyakarta. Merapi and its neighboring volcano Merbabu (3,118 m a.s.l.), are the highest peaks in the surrounding areas, causing strong gradients in phase delays. Second, we will compare the performances of atmospheric corrections derived from global weather-based models and local GNSS tropospheric delays. The selection of the two test sites is motivated by the fact that they represent two end-members in terms of ground instrumentation. On the one hand, Piton de la Fournaise is one of the most instrumented volcanoes in the world with 41 GNSS stations distributed on La Réunion Island during our period of survey (Figure 1a, Table 1). It will be an analogue to other well-instrumented volcanoes such as Etna and Kilauea. On the other hand, Merapi had 8 GNSS stations up-running during our period of survey (Figure 1b and Table 1). For the two scenarios, we will propose an adapted workflow describing how to use the GNSS ZTD measurements to improve the quality of atmospheric corrections.

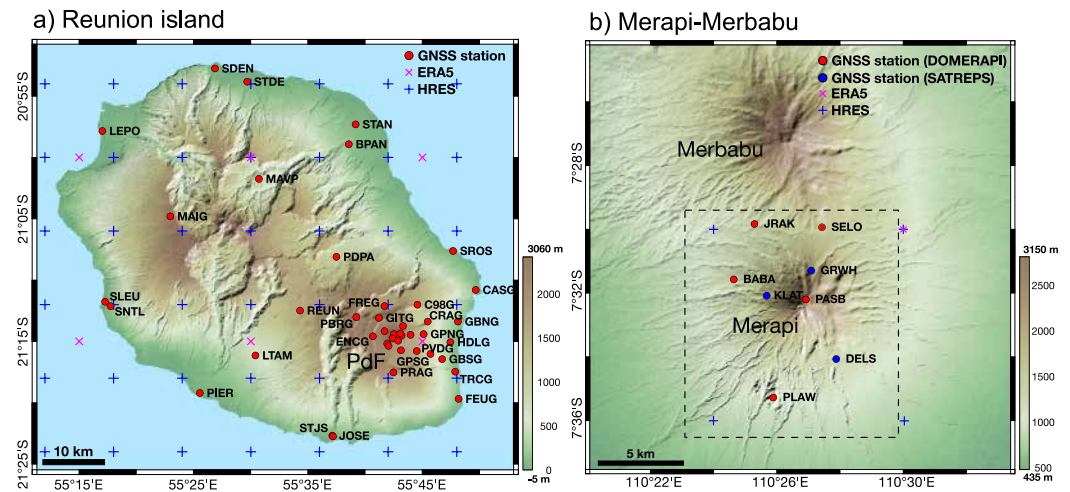


Figure 1. Topographic maps showing the distribution of the GNSS networks and the grids of the ECMWF products (ERA5 in purple and HRES in blue) for the two test sites: (a) La Réunion Island with a total of 41 GNSS stations during the period of survey: 25 operated by the Observatoire Volcanologique du Piton de la Fournaise (OVPF) and 16 by other institutions (Pdf refers to Piton de la Fournaise). and (b) the Merapi-Merbabu area with 8 GNSS stations operated on the Merapi flanks by the Center for Volcanology and Geological Hazard Mitigation (CVGHM) during the period of survey. The dashed rectangle indicates the area restricted on the Merapi volcanic edifice.

2. Test Sites

Oceanic volcanic islands (e.g., Hawaii, La Réunion) and high-elevated stratovolcanoes located in tropical regions (e.g., Indonesia and Central America) are places where strong atmospheric signals are often present in InSAR data (Albino et al., 2020; Cao et al., 2021; Ebmeier et al., 2013). Such atmospheric artifacts can limit the detection of ground deformation signals and therefore efficient corrections are required. In our study, we select two test sites located in tropical environments that have different characteristics in terms of topography, spatial extent, climate and number of GNSS stations available.

2.1. La Réunion Island

The first test site is La Réunion Island, located in the Indian Ocean at 700 km East from Madagascar (Figure 1a). The current volcanic activity focuses on Piton de la Fournaise, a shield volcano (2,632 m a.s.l.) covering the eastern third of the island. Piton de la Fournaise is very active with 1–2 eruptions (VEI 0–1) every year on average since 1972 (Peltier et al., 2009), with the last one that occurred from 2 July to 10 August 2023 at the time of writing. The climate is hot sub-tropical with a cyclone season from December to April. The real-time monitoring of Piton de la Fournaise is operated by the “Observatoire Volcanologique du Piton de la Fournaise” (OVPF) from Institut de Physique du Globe de Paris and the volcano is well-instrumented with a dense network of ~ 106 sensors deployed in the field among which 25 GNSS stations over the island. OVPF also used and processed the data of 16 additional GNSS stations operated by its partners: Lél@ (BPAN, JOSE, LTAM, MAVP, PDPA, SDEN, SLEU), TERIA (LEPO, PIER, SNTL, SROS, STAN, STDE, STJS), IGN (REUN) and the LACy laboratory from Université de la Réunion (MAIG). Frequent magma injections at Piton de la Fournaise induce strong ground deformation signals (a few 10 cm) on interferograms that can be detected without applying atmospheric corrections (Richter & Froger, 2020). Between inter-eruptive periods, radial displacements of a few cm/yr are often detected by GNSS time series (Staudacher & Peltier, 2015). Such signals are interpreted as the pressurization of the shallow magma reservoir that is connected to a deep reservoir (Peltier et al., 2016). So far, the inter-eruptive

Table 1
Characteristics of the GNSS and SAR Data Sets for the Two Sites

Target	La Réunion Island	Merapi-Merbabu
Name	La Réunion Island	Merapi-Merbabu
Period of survey	2021	2016–2018
Survey area (km ²)	2,512	8,928
GNSS data set		
Number of stations available	41	8
Average distance ^a (km)	8.2	5.3
Min elevation (m)	15.6	1,235
Max elevation (m)	2,579.2	2,676
InSAR ascending data set		
Number of interferograms	115	192
Time of acquisition (UTC/local)	14:53/18:53	10:58/17:58
InSAR descending data set		
Number of interferograms	108	105
Time of acquisition (UTC/local)	1:47/5:47	22:17/5:17

^aAverage distance is calculated from a Delaunay triangulation.

signals have not been detected by InSAR and therefore the production of accurate local atmospheric models would help to reduce the detection threshold.

2.2. Merapi-Merbabu Area

The second test site is centered on the Merapi and Merbabu volcanoes which are located in Java (Indonesia), 22 km North from the city of Yogyakarta. Merbabu has been inactive since 1797 whereas Merapi is a strato-volcano (2,910 m a.s.l.) that has been active for 100,000 years (Gertisser et al., 2012). At Merapi, the last major explosive eruption (VEI 3–4) took place in November 2010 (Surono et al., 2012). Activity resumed in 2018–2019 and the volcano has been intermittently active since 2020. The climate is tropical rainforest with a rainy season between the end of October and April. Due to the high elevation of the two volcanic edifices, we expect the atmospheric noise in interferograms to be dominated by the stratified component.

The real-time monitoring of Merapi is operated by the Center for Volcanology and Geological Hazard Mitigation (CVGHM). The Merapi volcano is less instrumented than Piton de la Fournaise with only 8 GNSS stations on the Merapi's flanks during the period of survey (Figure 1b) (Budi-Santoso et al., 2023). Three stations were installed in 2011 under the Indonesia-Japan project SATREPS (blue dots in Figure 1b) and five additional stations were later installed in 2013 during the France-Indonesia project DOMERAPI (red dots in Figure 1b). At Merapi, as on many other andesitic stratovolcanoes, DInSAR faces several challenges hindering an easy understanding of volcanic unrest. The limiting factors are strong tropospheric signals along with small and localized deformation in the near-field of the volcano summit. It results in a very low signal-to-noise ratio and therefore, it is crucial to develop the most accurate tropospheric corrections to better characterize ground movements.

3. Data Sets and Methods

3.1. Sentinel-1 SAR Data

We use Sentinel-1 SAR data freely provided by the European Copernicus program. For La Réunion Island, the minimum revisit time is 12 days for both descending and ascending acquisitions. Wrapped and unwrapped interferograms were processed for the year 2021 by the LiCSAR automated system (Lazecký et al., 2020). Unwrapped interferograms are multi-looked (20 times in range and 4 times in azimuth), geocoded and finally resampled to a spatial resolution of 90×90 m. For the time series, the network of interferograms is composed of 3–4 close pairs with a total of 115 and 108 interferograms for the ascending and descending tracks, respectively (Table 1, Figure S1 in Supporting Information S1). During the period of the survey, three dyke intrusions occurred on Piton de la Fournaise successively on 09 April, 18 October and 22 December causing step-like displacements in a few GNSS time series located at Enclos Fouqué.

For Merapi-Merbabu, we chose to conduct the study between January 2016 and June 2018, a period during which the GNSS time series has not detected deformation. On this basis, we assume that the phase differences observed on interferograms are mainly due to atmospheric noise. Sentinel-1 wrapped and unwrapped interferograms were processed using the NSBAS processing chain (Doin et al., 2011). temporal frequency of the SAR acquisitions is not constant throughout the period. The revisit time is 24 days for both ascending and descending tracks for the year 2016. Starting in March 2017, both tracks show at least two acquisitions per month. After August 2017, the revisit time of the ascending track decreases to 6 days thanks to Sentinel-1B. As a result, the interferogram network is quite different for the two tracks with 192 ascending and 105 descending interferograms (Table 1, Figure S2 in Supporting Information S1). Unwrapped interferograms are multi-looked (32 times in range and 8 times in azimuth), geocoded, and oversampled to a spatial resolution of 30×30 m to match the spatial resolution of SRTM DEM (1 arc second). GACOS products have also been resampled to this resolution.

3.2. Phase-Elevation Empirical Corrections

Phase-elevation empirical method was the first one to be implemented for correcting atmospheric phase delays on individual interferograms. It is based on the assumption that there is a correlation between the tropospheric phase delays and the elevation. Since the 1990s, this approach has been implemented on several volcanoes (Remy et al., 2003; Wicks Jr et al., 2002). The first step consists of estimating the relationship between the phase of the interferogram and the elevation. The choice of the fitted function is dependent on the studied area and several functions have been tested (linear, power-law or cubic splines) in previous studies. The best-fit parameters can be

evaluated either on the entire interferogram covering hundreds of kilometres or at smaller scales using sub-sampling windows or segmentation approach (Béjar-Pizarro et al., 2013; Bekaert et al., 2015; Elliott et al., 2008; Murray et al., 2020). As a result, a model of tropospheric delays is produced for each interferogram using DEM values and the best-fit parameters values as inputs.

The main advantage is that the method is simple to implement as it only requires a DEM of the area, the model is fast to calculate as it relies on least squares inversion of few parameters and final products have the same resolution as the DEM. However, the method has several limitations: first, it will only correct the stratified component of the tropospheric delays and more importantly it can remove part of the ground deformation signals that correlate with topography unless a joint inversion is used to retrieve both tropospheric delays and ground measurements by assuming a model of deformation (Beauducel et al., 2000).

The use of the phase-elevation empirical approach on single interferograms is not recommended for strato-volcanoes such as Merapi as the deformation signals of a shallow spherical source and stratified delays can show similar patterns (Rémy et al., 2015; Yip et al., 2019). For this reason, we only tested the performance of this approach for Piton de la Fournaise by considering a linear relationship calculated on La Réunion Island.

3.3. Weather-Based Corrections Based on ECMWF Products

The European Center for Medium-Range Weather Forecasts (ECMWF) performs weather's global forecast at medium-range (10-day) and long-range (1–3 months), through its Integrated Forecasting System (IFS), an approach combining numerical atmospheric models and data assimilation. For the data assimilation, ECMWF weather-based models use GNSS stations that belong to the International Ground Station network (IGS). For each of our test sites, there is only one IGS station available: (a) station Le Tampon (REUN00REU) located in the center of La Réunion Island and (b) station Yogyakarta (JOG200IDN) located in the capital city ~25 km from Merapi's summit. In addition, the ECMWF uses the IFS to carry out the reanalysis of archived observations that are useful for monitoring climate change. Climate reanalysis provides a set of parameters at each location on Earth such as air temperature, pressure and wind at different altitudes, and surface parameters such as rainfall, soil moisture content ocean-wave height and sea-surface temperature.

One of the most used ECMWF products is the fifth-generation atmospheric reanalysis, called ERA5, which replaces ERA-Interim from 31 August 2019. It provides hourly solutions of atmospheric conditions from the year 1959 onwards on a $0.25 \times 0.25^\circ$ lat/lon grid (~30 km), using 137 levels from the surface to a height of 80 km. Preliminary daily updates are available within 5 days of real-time but quality-assured monthly updates are delivered within 3 months of real-time. In addition to ERA5, a high-resolution 10-day forecast (HRES) is produced four times a day (0/6/12/18 hr UTC) on a $0.1 \times 0.1^\circ$ lat/lon grid (~10 km), using 137 levels in the vertical. Analysis data sets are available with a minimum latency of 5 hr 40 min for runs 0/12 and 11 hr 35 min for runs 6/18hr. Such data sets are used as inputs by the Generic Atmospheric Correction Online Service (GACOS) developed by the University of Newcastle to produce on-demand Zenith Tropospheric Delay (ZTD) maps at a spatial resolution of 90 m for any specific location and date of acquisition (Yu, Li, Penna, et al., 2018). GACOS performs an Iterative Tropospheric Decomposition (ITD) of the total delays to better estimate both the stratified and turbulent components (Yu, Li, & Penna, 2018). Although ECMWF HRES are available within a few hours, GACOS delay maps can only be obtained for dates that are at least 4 days before the current day.

The main advantage of ECMWF models is to provide information about atmospheric conditions at any location based on the assimilation of a large amount of data acquired from satellites and ground stations. In addition, the tropospheric delays obtained from such models are fully independent of the DInSAR measurements. Therefore, this method is well adapted for correcting tropospheric delays for regional or global surveys. However, due to their coarse spatial resolution (10 or 30 km), these products are less adapted for mitigating tropospheric delays on volcanoes. In addition, the method is not optimal for near real-time monitoring, as the time latency to obtain the products is about a week. Finally, the accuracy of the weather model is dependent on the set of observations available and their associated errors, therefore the quality will vary significantly from one site to the other.

In our study, ERA5 Zenith Tropospheric Delays (ZTD) are derived using the NSBAS processing pipeline (Doin et al., 2009; Jolivet et al., 2011). ZTD maps are derived from the vertical profiles of temperature, specific

humidity and geopotential height on pressure levels at points of the ERA5 grid located in the SAR scene for the hourly solution that is closest in time to the time of the SAR acquisition. Integrated delays obtained at each node are then spatially interpolated both horizontally and along elevation profiles to obtain a map of the tropospheric delay. For each interferogram, the ERA5 correction is computed by differentiating the tropospheric delay maps of the two epochs. Products computed in the zenith direction are then projected into the line-of-sight (LOS) using the map of incidence angle. For Piton de la Fournaise, ERA5 delay maps were geocoded at the same spatial resolution as the LiCSAR unwrapped interferograms; for Merapi, ERA5 delay maps were used before unwrapping to reduce unwrapping errors on the highest slopes of the volcano. From both test sites, GACOS Zenith Tropospheric Delays maps were requested through the online platform (<http://www.gacos.net/>) at the time of each SAR acquisition. Similarly to ERA5, the GACOS corrections are obtained by calculating the difference between two ZTD epoch maps and re-projecting them into the corresponding LOS.

3.4. Local Corrections Based on GNSS Zenith Tropospheric Delays

On active volcanoes, local networks of GNSS stations are installed and operated by Volcano Observatories to monitor ground displacements at high temporal resolution (30 s to daily solutions). However, the transmission of the signal between the satellites and the GNSS receivers is impacted by the atmospheric layers. Assuming that the position of the GNSS station is stable for a period of 24hr, Zenith Tropospheric Delays solutions can be inferred with a temporal sampling ranging from 5 min to 1 hr.

Compared to weather models, ZTD measurements derived from the GNSS data set can be obtained as soon as data are processed with a latency <1 hr. For this reason, the GNSS approach is more suitable than weather models for performing routine atmospheric corrections in the framework of InSAR near real-time monitoring. ZTD measurements at each GNSS station are expected to be much more accurate than interpolated ZTD inferred from global ECMWF models. As a result, it is possible to use GNSS-derived ZTD maps to efficiently correct small wavelength signals. With the high temporal sampling of GNSS ZTD maps, we can also expect to better track turbulent disturbances in the atmospheric conditions. However, the benefit of the method will depend on the number of GNSS stations and their spatial distribution.

Here, we will test the benefit of GNSS ZTD measurements in comparison with the two other approaches (e.g., empirical and weather-based models) by considering two end-members: (a) a dense network of 41 stations with the Piton de la Fournaise volcano and (b) a coarse network of 8 stations with the Merapi volcano.

At La Réunion Island, GNSS RINEX files are processed using the GAMIT software (Herring et al., 2010). The data processing enables us to retrieve the position of each station using the Precise Point Positioning (PPP) mode and to derive hourly solutions of the Zenith Total Delays (ZTD) assuming a fixed daily position (Figure S5 in Supporting Information S1). At Merapi, GNSS data are processed with the Jet Propulsion Laboratory's software package Gipsy-X using PPP mode to derive 5 min ZTD solutions (Bertiger et al., 2020). For each data set, we use the ZTD measurements that are close in time to each SAR acquisition. For La Réunion Island, we do not perform any temporal interpolation as the time lag between GNSS and SAR measurements is 7 min for the ascending orbit and 13 min for the descending orbit (Table 1).

To derive a ZTD delay map from GNSS sparse measurements, we apply the Iterative Tropospheric Decomposition strategy (Yu et al., 2017; Yu, Li, & Penna, 2018). The method takes the advantage that the total delay can be decomposed into two independent components: (a) a Zenith Stratified Delay (ZStD) that is a function of the elevation and (b) a Zenith Turbulent Delay (ZTuD) considered as the residual signal. The ITD procedure can be summarized as the four following steps.

1. ZTD measurements at the test site are fitted as a function of the elevation using the exponential function:

$$ZTD = ae^{-bZ'} \quad (1)$$

where Z' is the normalized elevation $Z' = \frac{Z_{GNSS}}{\max(Z_{DEM}) - \min(Z_{DEM})}$. The parameter Z_{GNSS} corresponds to the elevation of the station whereas $\min(Z_{DEM})$ and $\max(Z_{DEM})$ are the minimum and maximum elevation values of the studied area derived from the SRTM DEM.

1. the retrieved values, a and b , and the normalized elevation Z' of the SRTM DEM are substituted in Equation 1 to produce a map of the stratified delay (ZStD).
2. the residual is calculated at each station by differencing the processed ZTD and the estimate of ZStD; the map of the Zenith Turbulent Delay (ZTuD) is obtained by performing spatial interpolation. Different interpolation methods have been tested (e.g., linear, Inverse Distance Weighting, kriging or natural neighboring) and natural neighbor is providing the best results.
3. for each epoch, ZTuD and ZStD maps are added to obtain a final ZTD map having the spatial resolution of the DEM.

For each interferogram, the corresponding GNSS model is obtained by differentiating ZTD maps of the corresponding epochs and by converting the ZTD difference into Slant-range Tropospheric Delay (STD) difference using the incidence angle of Sentinel-1 acquisitions.

For La Réunion Island, the method proposed is well adapted as the GNSS network is dense enough (41 stations). Either the stratified or the turbulent component will dominate the computed STD map depending on the period covered (Figure S3 in Supporting Information S1). For the year 2021, some gaps exist in the ZTD time series for several GNSS stations due to technical issues. In addition, we apply a filter for only keeping ZTD measurements with a standard deviation smaller than 1 cm (e.g., an uncertainty $<0.5\%$ considering a ZTD of 2 m). As a result, the final number of stations used to compute the GNSS models varies between 21 and 39 stations depending on the epoch with an average of 34 stations for both ascending and descending tracks (Figure S4 in Supporting Information S1).

For the Merapi volcano, we find that the spatial interpolation of the turbulent part (ZTuD) does not provide relevant results as it introduces noise in the corrected interferograms. For the Merapi volcano, we adapt the proposed method using only steps 1–2 to characterize the stratified part and consider no turbulent residual in the GNSS model. At first order, this is acceptable as stratified signals dominate phase delays for 95% and 85% of the ascending and descending interferograms, respectively (e.g., correlation coefficient >0.7 , and phase-elevation slope >5 rad/km). Because the quality of zenith tropospheric delays varies between the two networks installed at Merapi, we chose to weight the ZTD values according to their standard deviation during the fitting of the stratified component. We recommend this approach for combining data sets derived from different campaigns or processing, and for sites in which the number of GNSS stations is limited.

3.5. Statistics Analysis

To assess the performance of the different corrections, several criteria must be evaluated such as the reduction of the standard deviation and the reduction of the phase-elevation correlation (Albino et al., 2020; Murray et al., 2019; Stephens et al., 2020).

3.5.1. Reduction of the Standard Deviation

Assuming there is no deformation signal, the spatial variability of the phase difference in an interferogram is dominated by tropospheric noise in comparison with other sources of noise (e.g., DEM errors and orbital errors). Therefore, the performance of the correction can be quantified by evaluating the relative difference in the standard deviation between the unwrapped raw interferogram and the unwrapped corrected interferogram:

$$Q1 = -\frac{(\sigma_f - \sigma_i)}{\sigma_i} \quad (2)$$

where σ_i and σ_f are the standard deviations of the raw and the corrected unwrapped interferogram, respectively.

The minus sign is used to obtain a positive value of $Q1$ for cases in which there is a reduction of the standard deviation after correction. The value $Q1 = 1$ corresponds to an ideal case for which the corrected interferogram is noise-free (e.g., a flat interferogram with a constant value for all pixels). Negative values of $Q1$ indicate poor performance as the correction increases the noise level and therefore corrections should not be applied.

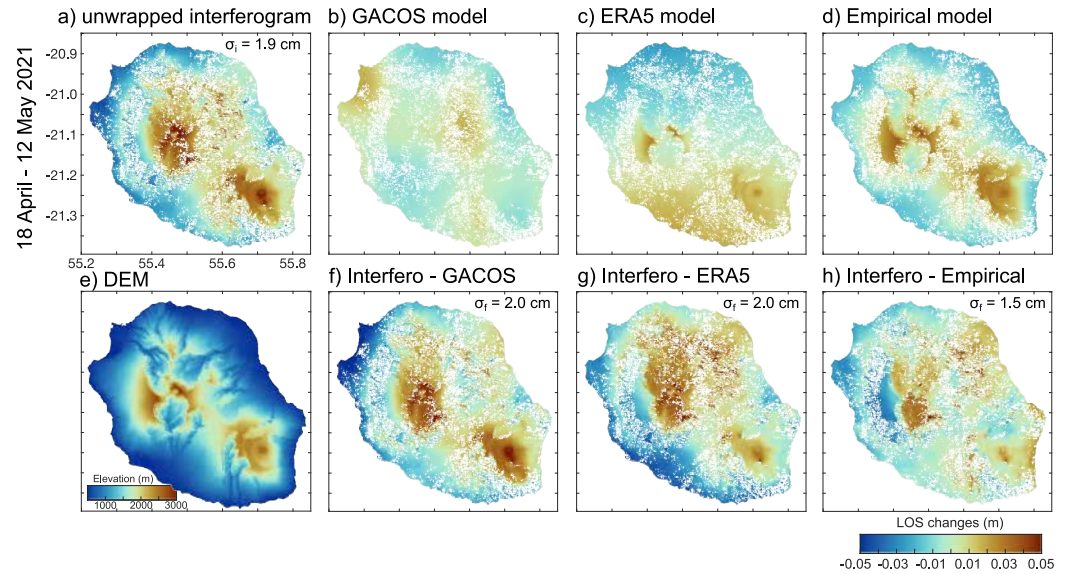


Figure 2. Comparison of the different methods for correcting tropospheric delays on an individual interferogram covering La Réunion Island, processed between 18 April and 12 May 2021. (a) Unwrapped interferogram before correction; (b–d) tropospheric delays derived from (b) GACOS model, (c) ERA5 model and (d) empirical phase-elevation correlation. (e) Digital Elevation Model of the island; (f)–(h) Corrected interferograms after applying the three different corrections.

3.5.2. Reduction of the Phase-Elevation Correlation

We evaluate the phase-elevation correlation with a linear fit: $\delta\phi = aZ + b$, where Z corresponds to the elevation and $\delta\phi$ the phase of the unwrapped interferogram. As a second criterion $Q2$, we quantify the relative reduction of the phase-elevation correlation:

$$Q2 = -\frac{|a_f| - |a_i|}{|a_i|} \quad (3)$$

where $|a_i|$ and $|a_f|$ are the absolute values of the slope for the raw and the corrected unwrapped interferogram, respectively.

Contrary to the criterion $Q1$ that considers the reduction of the total tropospheric signal, the criterion $Q2$ will provide the performance of each approach to correct the stratified component of the signal. For $0 < Q2 < 1$, the correction applied removes part of the stratified signal ($Q2 = 1$ being the case for which there is no phase-elevation correlation in the corrected interferogram). For negative values of $Q2$, the correction applied adds some stratified signals that were not present in the original interferogram.

For the empirical method, the criterion $Q2$ is equal to 1 for all interferograms, as the method relies on the phase-elevation correlation, so it serves as a reference for comparison. However, an interferogram with $Q2 = 1$ does not mean a perfect correction, as large turbulent signals can still be present in the corrected interferograms. For ERA5 and GACOS weather-based corrections, the criterion $Q2$ will vary among the interferograms.

4. Performance of Common Atmospheric Corrections

4.1. Test Site 1: La Réunion Island

4.1.1. Performance of the Corrections on Individual Interferograms

Based on the analysis of our data set, atmospheric noise in La Réunion is dominated by: (a) stratified signals related to the topography of the island and (b) large wavelength signals related to the climate and the amount of rainfall in the island.

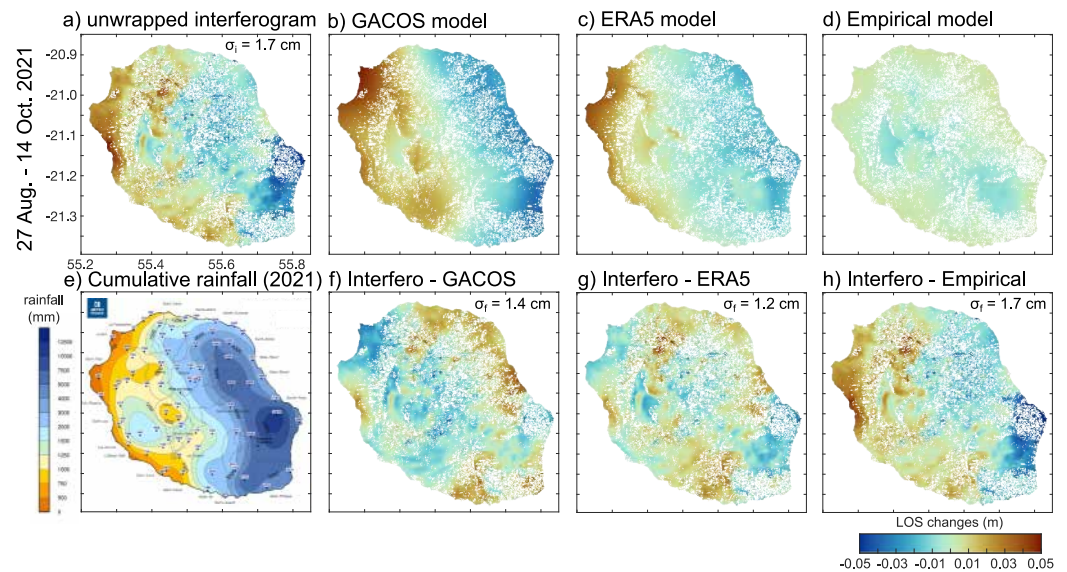


Figure 3. Comparison of the different methods for correcting tropospheric delays on an individual interferogram covering La Réunion Island, processed between 27 August and 14 October 2021. (a) Unwrapped interferogram before correction; (b–d) tropospheric delays derived from (b) GACOS model, (c) ERA5 model and (d) empirical phase-elevation correlation. (e) Cumulative rainfall for the year 2021 provided by Meteo France; (f)–(h) Corrected interferograms after applying the three different corrections.

Figure 2a shows an unwrapped interferogram with a strong stratified signal ($\sigma_i = 1.9$ cm). In the first order, the tropospheric signal correlates with the topography of La Réunion Island (Figure 2e). Therefore, the empirical model provides a good fit (Figure 2d), with a reduction of the standard deviation of $Q1 = 0.21$ (Figure 2h). However, small negative and positive signals remain after the correction on the SW and NE coasts, respectively. For this example, both delay maps derived from the two weather models (GACOS, ERA5) (Figures 2b and 2c) do not reproduce the stratified component. The weather-based corrections perform poorly, as they increase the standard deviation from 1.9 to 2.0 cm ($Q1 = -0.05$). In this case, it is not recommended to perform such weather-based corrections as they would increase the tropospheric noise in the data.

Figure 3a shows an unwrapped interferogram with large wavelength signals ($\sigma_i = 1.7$ cm). The spatial pattern corresponds to a SW-NE gradient that is partly correlated with the pattern of the annual rainfall recorded in 2021 over the island (Figure 3e). The SW section is the downwind side and it corresponds to the driest part of the island with less than 1,000 mm of rainfall per year whereas the NE section is the upwind side that receives a large amount of rainfall between 2,000 and 12,000 mm per year.

In this case, both weather-based models (GACOS, ERA5) can mimic the long wavelength signals observed in the interferogram (Figures 3b and 3c). Overall, the performance of the corrections is good with a reduction of the standard deviation: from 1.7 to 1.4 cm for the GACOS model ($Q1 = 0.18$) and from 1.7 to 1.2 cm for the ERA5 model ($Q1 = 0.29$). Here, the ERA5 model performs $\sim 10\%$ better than the GACOS model. With $Q1 = 0$, the empirical model is not able to correct any of the long-wavelength signals present over the island (Figures 3d–3h).

Figures 2 and 3 show the large variability of tropospheric signals present at La Réunion Island and it demonstrates that the systematic correction based on a single approach (weather-based model or empirical) is not optimal for mitigating tropospheric signals.

4.1.2. Statistic Analysis of Weather-Based Corrections

Here, we assess the performance of global weather-based models during the year 2021 by quantifying the two criteria of quality ($Q1$ and $Q2$) described in Section 3.5. Our data set consists of 83 ascending and 108 descending unwrapped interferograms showing an initial average standard deviation of 2.3 and 1.9 cm, respectively. This difference is due to the daily variations of the atmospheric water vapor content, which are larger during the late

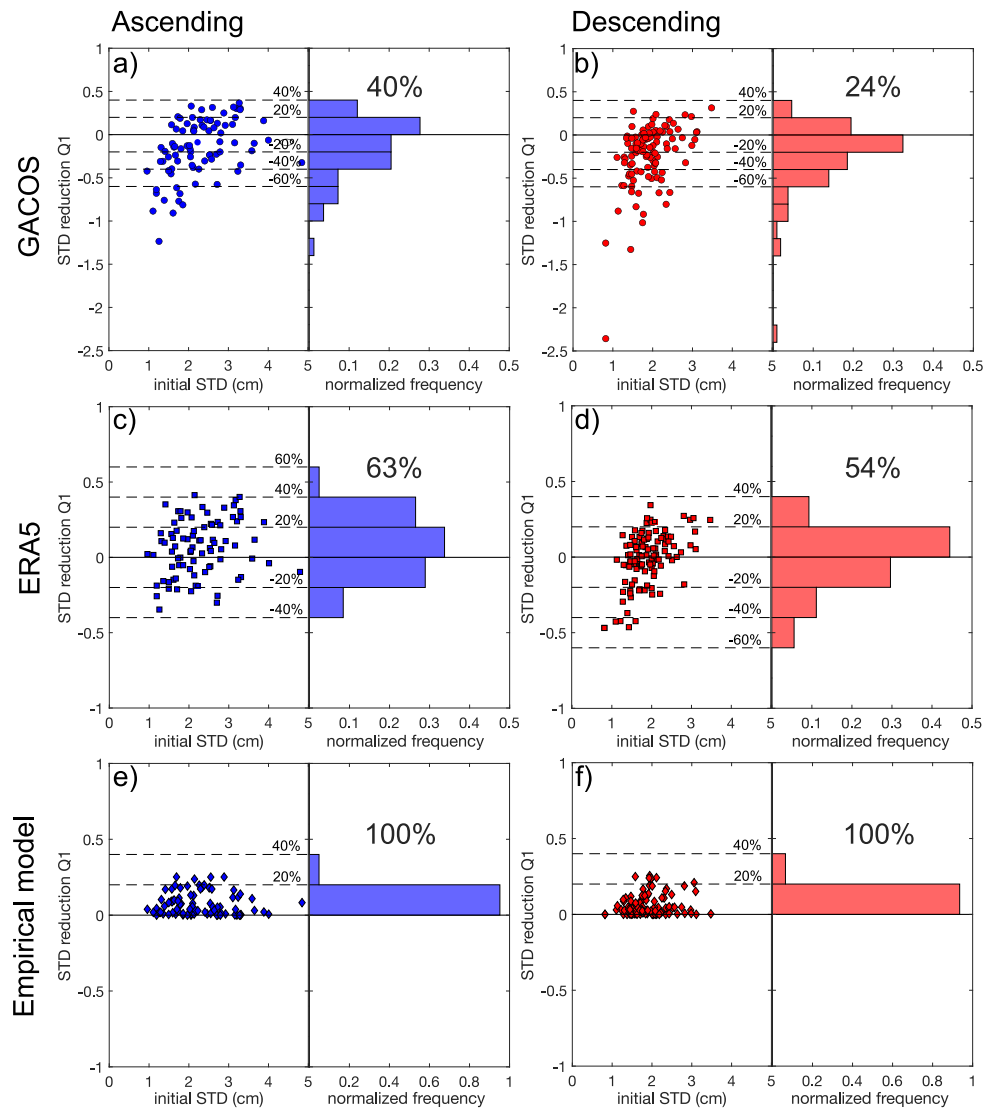


Figure 4. Reduction of the standard deviation $Q1$ as a function of the initial standard deviation of the interferograms for the ascending (blue) and the descending (red) data set for La Réunion Island. We compare the three methods: (a–b) GACOS model, (c–d) ERA5 model and (e–f) empirical model.

afternoon (18 hr 53 min - ascending path) than during the early morning (5 hr 47 min-descending path). This phenomenon is even more pronounced during the rainy months between January and March.

GACOS corrections show poor performance with a reduction of the standard deviation ($Q1 > 0$) for only 40% of the ascending interferograms and 24% of the descending interferograms (Figures 4a and 4b). It means that on average GACOS corrections increase the noise level in the data. Among the positive cases ($Q1 > 0$), the reduction of the noise $Q1$ remains small with average values of 17% and 11% for the ascending and descending data sets, respectively.

ERA5 corrections show average performance with a reduction of the standard deviation for more than half of the interferograms: 63% for the ascending track and 54% for the descending track (Figures 4c and 4d). Among the positive cases ($Q1 > 0$), the reduction of the noise for ERA5 corrections is on average similar to GACOS corrections, with values of 17% and 12% for the ascending and descending data sets, respectively.

Both weather-based models show better performance for the ascending data sets than for the descending data sets. Ascending data sets show more dispersion in the values of σ_i than descending data sets (Figures 4a and 4b); in

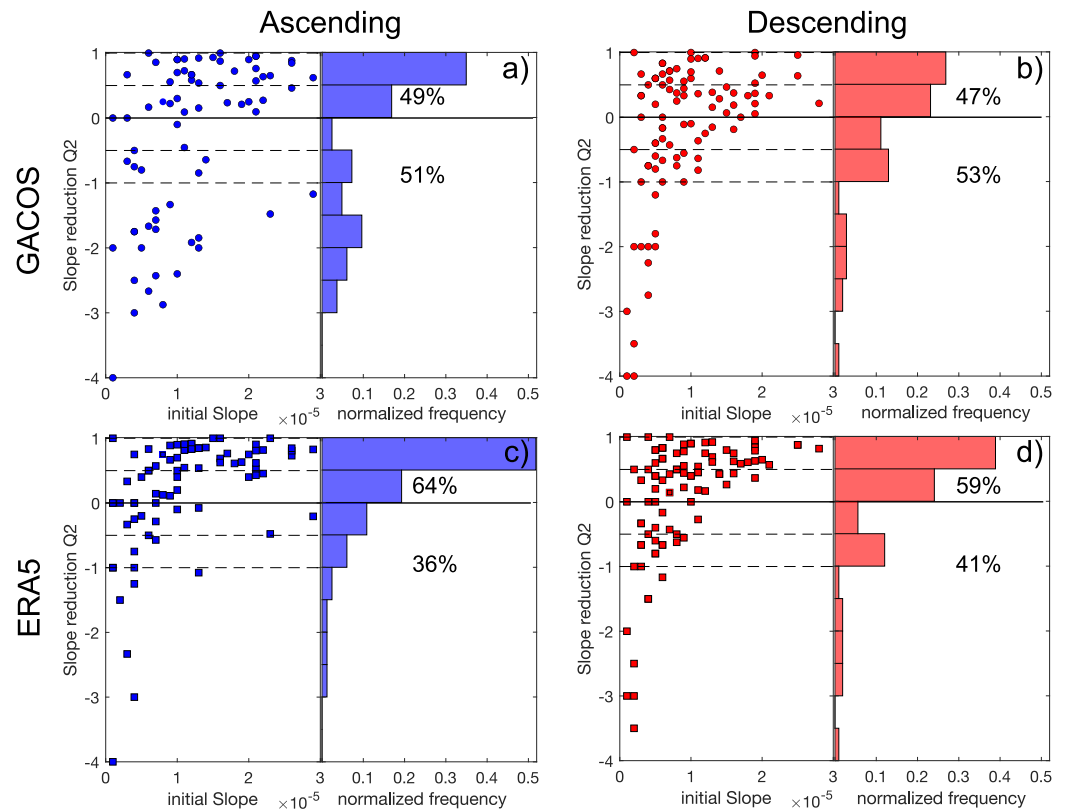


Figure 5. Reduction of the phase-elevation correlation $Q2$ as a function of the slope of the phase-elevation correlation of the raw interferogram for the ascending (blue) and the descending (red) data set for La Réunion Island. We compare the weather-based models (a–b) GACOS and (c–d) ERA5.

addition, 37% of the ascending interferograms contain strong tropospheric noise ($\sigma_t > 2.5$ cm) whereas this proportion only reaches 11% for the descending data sets. Statistically, it is more likely that corrections will be more effective for interferograms that contain initially strong tropospheric signals, explaining the difference in overall performance between descending and ascending data sets. Compared to weather-based models, the empirical phase-elevation corrections always decrease the standard deviation of the interferogram ($Q1 > 0$) but the amplitudes of the reduction are less than 20% for more than 90% interferograms. Average values of $Q1$ are about 8% and 6% for ascending and descending, respectively, which is twice smaller than values obtained from weather models.

For the criterion $Q2$, GACOS corrections show poor performance with a reduction of the slope ($Q2 > 0$) for less than half of the interferograms: 49% of the ascending interferograms and 47% of the descending interferograms (Figures 5a and 5b). ERA5 corrections show average performance with a reduction of the slope for 64% of the ascending interferograms and 59% of the descending interferograms (Figures 5c and 5d). In terms of amplitude, the slope has been reduced by more than 50% ($Q2 > 0.5$) for 50% of the ascending interferograms and 40% of the descending interferograms. Results show that on average ERA5 models are 12%–15% more efficient than GACOS models for removing the stratified tropospheric noise contained in raw interferograms.

In the absence of local measurements (sounding balloons, GNSS), the ERA5 weather models should be preferred to GACOS weather models or even empirical models for correcting tropospheric signals at La Réunion Island.

4.2. Test Site 2: Merapi-Merbabu

4.2.1. Performance of the Corrections on Individual Interferograms

Interferograms at the Merapi volcano show either strong stratified signals correlated to the topography (Figure 6) or small-amplitude short wavelength turbulent signals (Figure 7). Stratified artifacts are usually present on the two

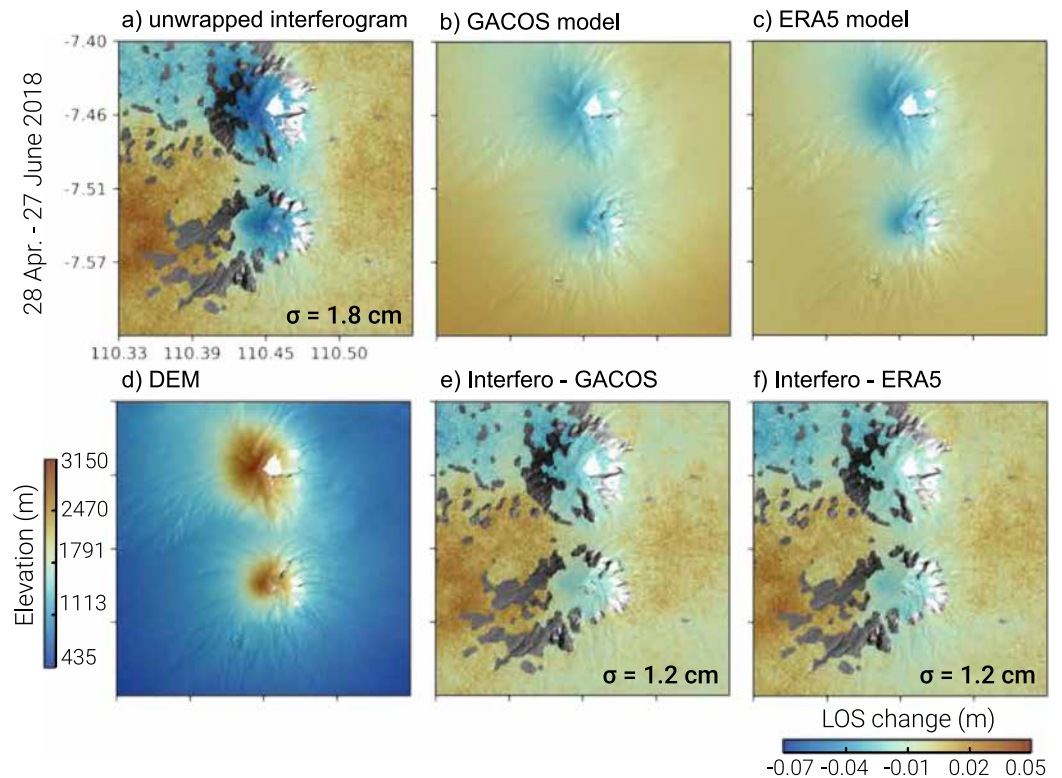


Figure 6. Comparison of the two weather-based methods for correcting tropospheric delays on an individual descending interferogram covering the Merapi area, processed between 28 April and 27 June 2018 showing strong stratified signals. (a) Unwrapped interferogram before correction; b,c: LOS tropospheric map delays derived from (b) GACOS model, (c) ERA5 model. (d) Digital Elevation Model of the area; (e), (f) Corrected unwrapped interferograms after removing the models. Areas with layover and unwrapping errors are masked and not considered for statistics.

neighbor volcanoes, Merapi and Merbabu, and are associated with two circular signals of a 30 km radius (Figure 6a). For this specific case, ERA5 and GACOS models correct efficiently the stratified signal contained in the raw interferogram (Figures 6b and 6c). However, both corrections slightly underestimate the amplitude of the signal and as a result, small residual signals remain at the volcanoes' summit in the corrected interferograms (Figures 6e and 6f). Here, the corrections show good performance with a reduction of standard deviation from 1.8 to 1.2 cm for both ERA5 and GACOS models ($Q1 = 0.36$). The stratified signals are largely reduced with $Q2 = 0.65$ and $Q2 = 0.57$ for ERA5 and for GACOS models, respectively.

For an interferogram dominated by small-scale turbulent signals, ERA5 and GACOS models do not correct efficiently the interferogram (Figure 7). Indeed, the reduction of noise shows values $Q1 = 0$ for GACOS and $Q1 = 0.07$ for ERA5 (Figures 7e and 7f). Regarding slope criteria $Q2$, the ERA5 model reduces most of the stratified component ($Q2 = 0.7$) observed in the two edifices (Figures 7c–7f) whereas the GACOS model adds stratified signal ($Q2 = -0.1$) that was not present in the raw interferogram (Figures 7b–7e).

The two examples show the variability of tropospheric signals observed on interferograms located at the Merapi-Merbabu volcanoes. It also highlights that weather-based models are not always consistent with each other and they do not systematically correct efficiently tropospheric signals observed in the raw data. Models can underestimate or overestimate the amplitude of stratified signals resulting in large residuals in the corrected interferograms.

4.2.2. Statistic Analysis of Weather-Based Corrections

At the Merapi volcano, the data set is composed of 105 descending interferograms and 192 ascending interferograms (Table 1). Based on the statistical analysis of the two criteria, $Q1$ and $Q2$, we can evaluate the performance of weather models at the scale of the Merapi-Merbabu volcanic area (Figure 1b).

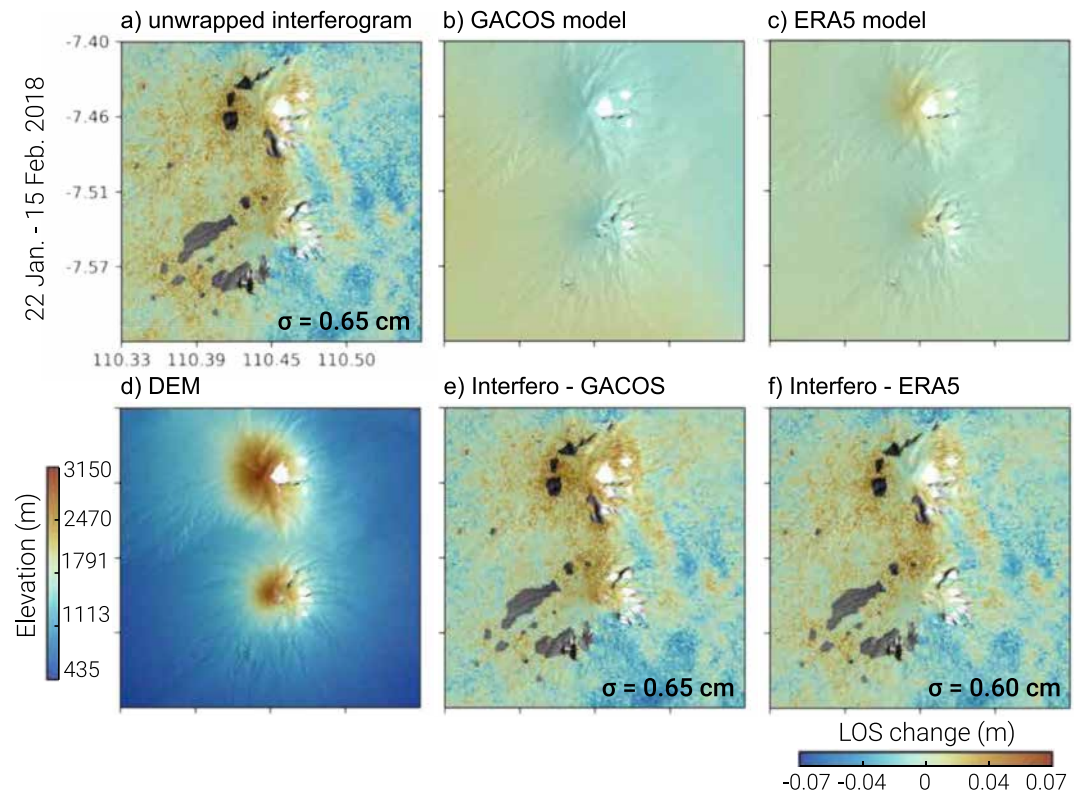


Figure 7. Comparison of the two weather-based methods for correcting tropospheric delays on an individual descending interferogram covering the Merapi area, processed between 22 January and 15 February 2018 showing small amplitude turbulent signals. (a) Unwrapped interferogram before correction; b,c: LOS tropospheric map delays derived from (b) GACOS model, (c) ERA5 model. (d) Digital Elevation Model of the area; (e), (f) Corrected unwrapped interferograms after removing the models. Areas with layover and unwrapping errors are masked and not considered for statistics.

For the ascending track, GACOS and ERA5 models reduce the standard deviation ($Q1 > 0$) for 36% and 51% of the interferograms processed, respectively (Figures 8a–8c). For the descending track, the proportion of efficient corrections is sensibly similar between the two models, with 41% for GACOS and 43% for ERA5 (Figures 8b–8d). Similar to Piton de la Fournaise, ERA5 models perform better than GACOS models for Merapi, especially for the ascending track for which the difference of performance reaches 15%. On the one hand, the distribution for ERA5 corrections is narrow and centered to $Q1 = 0$ with a large proportion of interferograms ($>80\%$) having values between -0.2 and 0.2 . On the other hand, GACOS corrections show a more asymmetric distribution toward negative values with almost 20% of interferograms with $Q1 < -0.2$.

For the ascending track, GACOS and ERA5 models reduce the phase-elevation correlation ($Q2 > 0$) for 37.5% and 59% of the interferograms, respectively (Figures 9a–9c). For the descending track, the proportion of efficient corrections is 49% for GACOS models and 66% for ERA5 models (Figures 9b–9d). Here, there is a net advantage for choosing ERA5 models over GACOS models as the difference of performance is $\sim 20\%$. For ERA5, one-third of the interferograms have $Q2$ values ranging between 0.5 and 1. This class corresponds to the maximum normalized frequency and the frequency decreases quickly as $Q2$ decreases. It underlines that ERA5 models are at first order an efficient approach to reduce part of the signals that correlate with topography at the scales of volcanic edifices. In comparison, the distribution of $Q2$ for GACOS is more uniform with a normalized frequency of ~ 0.2 for the three classes $[-0.5, 0]$, $[0, 0.5]$ and $[0.5, 1]$. As a consequence, GACOS corrections will add stratified noise for more than half of the interferograms. Such comparison shows that ERA5 models are much more adapted than GACOS for mitigating tropospheric stratified signals at Merapi, which is the same result previously found at Piton de la Fournaise.

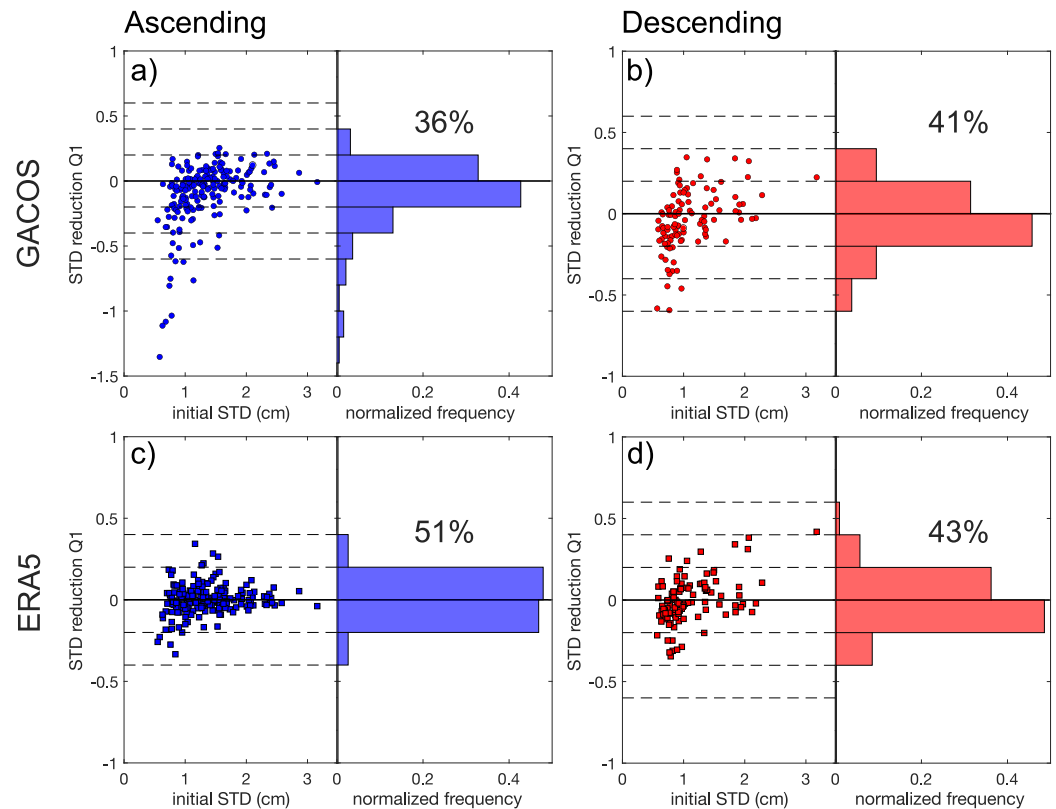


Figure 8. Reduction of the standard deviation Q1 as a function of the initial standard deviation of the interferograms for the ascending (blue) and the descending (red) data set at Merapi volcano. We compare the weather-based models: (a–b) GACOS and (c–d) ERA5.

4.3. Comparison Piton de La Fournaise Versus Merapi

For Piton de la Fournaise, results show that the performance is always higher for the ascending track than for the descending track, whatever the weather models used or the criteria chosen (symbol * in Table 2). Although the local time of SAR acquisitions is similar for the two test sites (Table 1), the results are different at Merapi. Except for the case Q1-ERA5, the descending track at Merapi shows better performance than the ascending track (* in Table 2), which is the opposite of what we observe at Piton de la Fournaise. Our results show that the influence of the timing of the SAR acquisitions on the performance of the corrections will be highly variable from one volcano to another.

Looking at the highest performance corrections (symbol * in Table 2), the values obtained in the ascending track at La Réunion Island are very similar to those obtained in the descending track at Merapi-Merbabu. It is a good estimation of the maximum performance we can expect on tropical volcanoes for correcting tropospheric signals using weather-based models. However, reaching at best 51% for the Merapi-Merbabu area and 63% for La Réunion Island on Q1, and respectively 66% and 64% for Q2, is not satisfactory. Therefore, in the next section, we will use local GNSS networks to produce tropospheric delay models and compare the performance we obtained with those from weather models.

5. Benefit of GNSS ZTD Measurements

5.1. Performance of the GNSS Corrections at La Réunion Island

We first apply the ITD method (Section 3.4) on GNSS stations at La Réunion Island to compute LOS phase delay maps for correcting the two individual interferograms previously shown in Figure 2a–3a. The GNSS model performs better than all three methods for correcting tropospheric signals correlated with topography (Figure 10 - top row). The standard deviation reduction is 37% that is 16% higher than the performance obtained with the

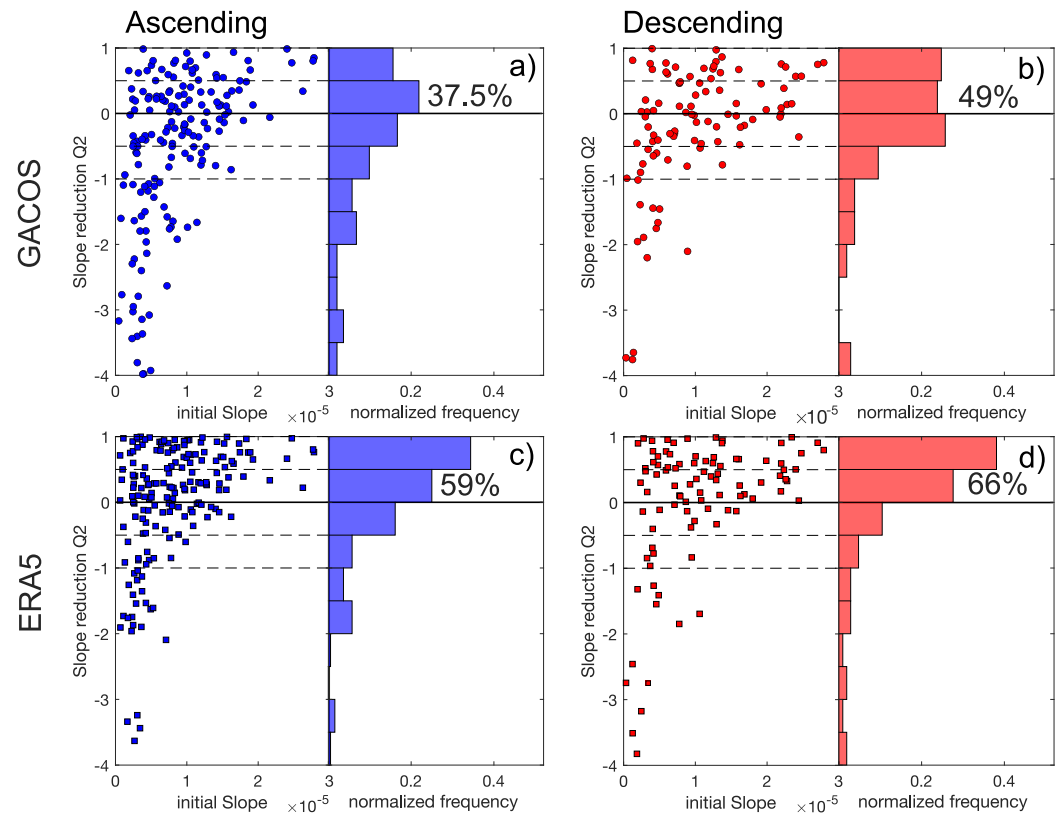


Figure 9. Reduction of the phase-elevation correlation Q2 as a function of the slope of the phase-elevation correlation of the raw interferogram for the ascending (blue) and the descending (red) data set at Merapi volcano. We compare the weather-based models (a–b) GACOS and (c–d) ERA5.

empirical approach (Figures 2d–2h). This is because the GNSS model can model the stratified signal as well as the phase ramp observed between the southwest and the northeast coastlines. The empirical method applied assigns the same phase delays along the coastlines (Figure 2d) and such SW-NE phase gradient can be removed only by applying additional ramp corrections. Compared to empirical methods, the GNSS model has the advantage of mitigating at once both stratified signals and long wavelength phase ramps. As the GNSS model is independent of the raw interferogram, our approach prevents the removal of ground deformation signals associated with the pressurization of magma systems.

Table 2

Performance of the Weather-Based Models for Ascending and Descending Data Sets Processed on the Two Test Sites

Weather models	Statistical metrics	La Réunion Island		Merapi-Merbabu area	
		Ascending	Descending	Ascending	Descending
GACOS	p (Q1>0) %	40*	24	36	41*
	median (Q1) %	−0.14*	−0.15	−0.04	−0.04
	p (Q2>0) %	49*	47	37.5	49*
ERA5	p (Q1>0) %	63*	54	51*	43
	median (Q1) %	0.07*	0.01	−0.002*	−0.02
	p (Q2>0) %	64*	59	59	66*

Note. Values correspond to the proportion of interferograms in per cent that is efficiently corrected based on the two criteria, Q1 and Q2. Symbol (*) indicates the maximum values between the two tracks. Areas considered are the ones displayed in Figure 1, respectively La Réunion Island and the Merapi-Merbabu area.

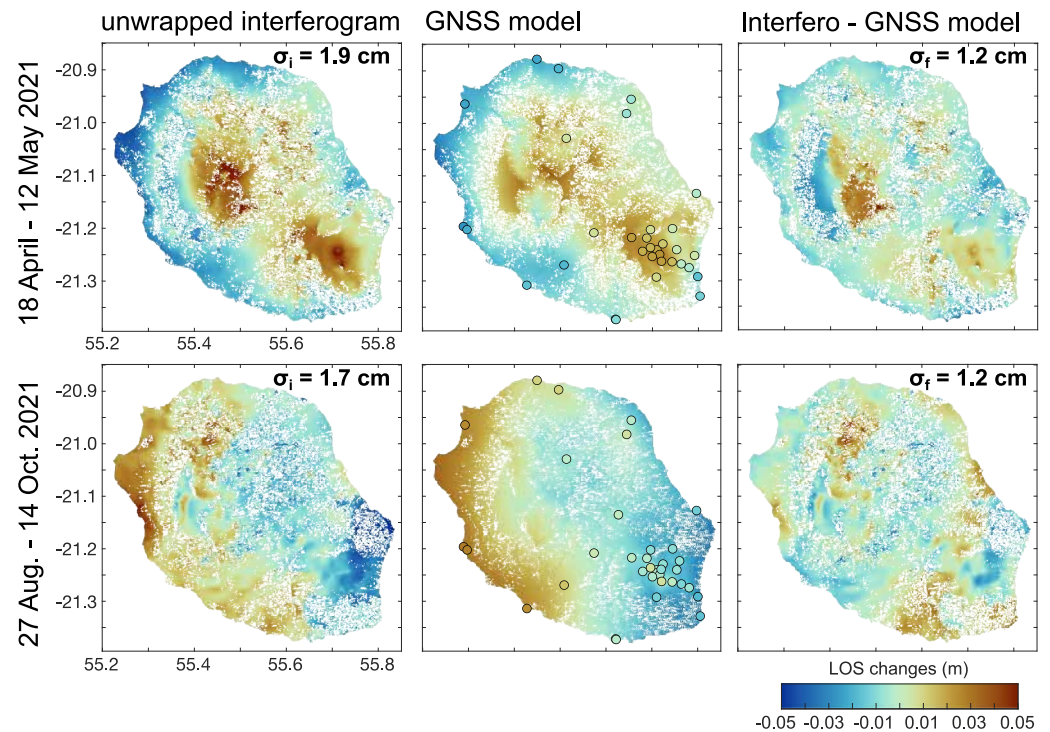


Figure 10. Performance of the GNSS models for correcting the two unwrapped interferograms shown in Figures 2a and 3a. The left panels show the unwrapped interferograms before correction. Middle panels are the models derived from the GNSS tropospheric total delays shown by the circles. The right panels correspond to the corrected interferograms after removing the GNSS models.

For the long wavelength signals caused by the spatial heterogeneities of the humidity over the island (Figure 10 - bottom row), the GNSS model performs better than the GACOS model (Figure 3b) and equally to the ERA5 model (Figure 3c). Here, the main advantage is that GNSS measurements are obtained in real-time and STD correction maps can be produced ~ 1 h after the SAR acquisition whereas ERA5 and GACOS products are available a few days after the SAR acquisition.

Then, we assess the performance of GNSS models by evaluating the criteria Q1 and Q2 over the ascending and descending data sets. GNSS models show very good performance with a reduction of the standard deviation after corrections for about 90% of the ascending interferograms and almost 78% of the descending interferograms (Figures 11a and 11b). Among positive cases ($Q1 > 0$), the average amplitude of the reduction of the standard deviation is 0.31 and 0.25 for the ascending and descending tracks, respectively. This is a significant improvement compared to previous methods that have an average reduction ranging between 0.08 and 0.18 (ascending) and 0.06–0.12 (descending).

GNSS models provide better results than global weather models for correcting stratified signals, with success rates of 75% and 69% for ascending and descending data sets, respectively (Figures 11c and 11d).

5.2. Performance of the GNSS Corrections at Merapi-Merbabu

Figure 12 shows the performance of GNSS models on the two individual interferograms previously shown in Figures 6a and 7a. For the first interferogram (28 April –27 June 2018), GNSS models perform 11% better than ERA5 and GACOS models with a reduction of the standard deviation of $Q1 = 0.44$. For the second interferogram (22 January–15 February 2018), the performance is equivalent to ERA5 models.

The performance of GNSS stratified models at the Merapi-Merbabu area is satisfactory, with a proportion of efficient corrections ($Q1 > 0$) for 54% of ascending interferograms and 43% of descending interferograms (Figure 13a–13c). By adding the turbulent component into the GNSS models (left panels), we see a large decrease

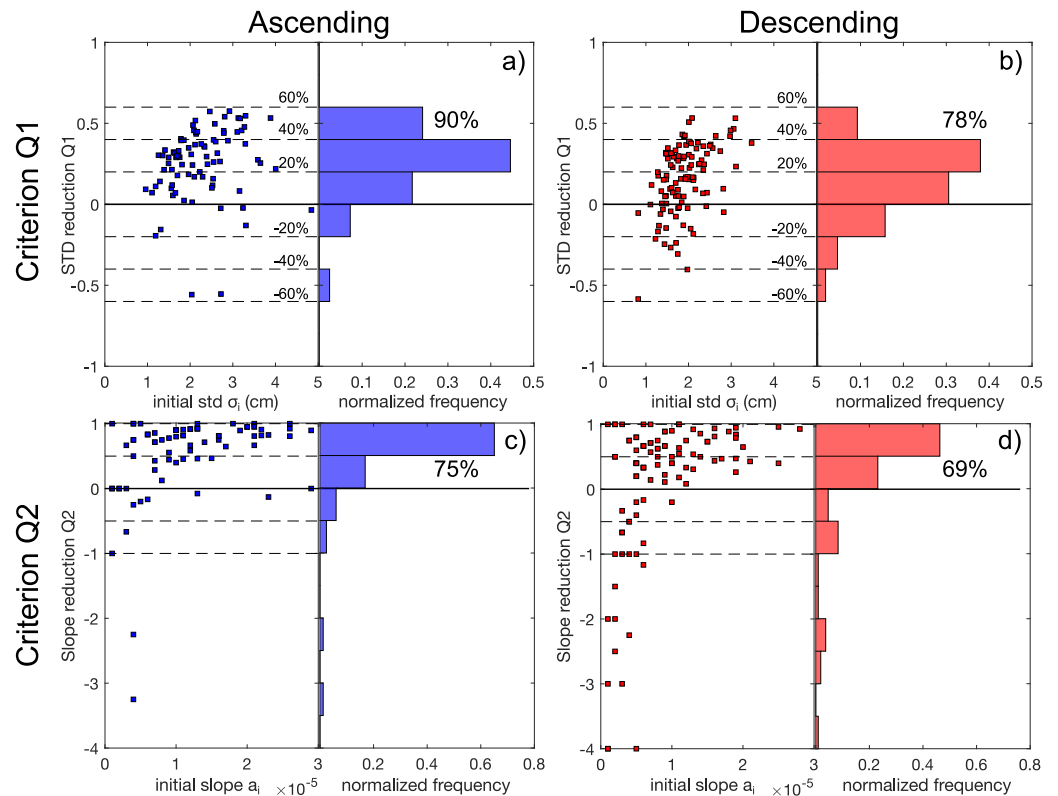


Figure 11. Performance of the GNSS STD maps evaluated at La Réunion Island through the statistics analysis of the two criteria of quality: (a–b) reduction of the standard deviation (Q1); (c–d) reduction of the slope of the phase-elevation correlation (Q2). Blue and red color correspond to the ascending and descending data set, respectively.

in the overall performance, which confirms that turbulent noise cannot be retrieved if the number of stations is too small. For the Merapi-Merbabu extent, GNSS stratified models perform equal to ERA5 models (51% and 43% for ascending and descending interferograms). By computing the statistics in the Merapi area where all the GNSS stations are located, the performances increase by 6%–7% compared to the Merbabu-Merapi extent (Figures 13d and 13f). GNSS stratified models are a better choice than ERA5 models only if we are looking at the local scale of the Merapi volcanic edifice.

5.3. Comparison Between Local GNSS Models and Global Weather-Based Models at the Two Test Sites

To discuss the benefit of GNSS models in comparison with weather-based models, we use Venn diagrams to evaluate if the different approaches provide redundant or additional information. For La Réunion Island, GNSS models provide significantly better performance than the two other methods, with an increase of ~50% compared to GACOS models (Figure 14a). For both tracks, the GACOS circle is encompassed by the ERA5 and GNSS circles (Figure 14a). It means that the GACOS models do not correct any interferograms that are not well corrected by the two other models. For 59% of ascending interferograms and 45.4% of descending interferograms, both ERA5 and GNSS models induce a reduction of the tropospheric noise. However, the amplitude of the reduction obtained with the GNSS model is larger than the ERA5 model for more than 80% of the cases. In addition, we observe that only a small fraction of interferograms are corrected by the ERA5 model and not by the GNSS model: 3.6% for ascending and 8.3% for descending. Therefore, our proposed strategy for well-instrumented volcanoes such as Piton de la Fournaise is to only use the GNSS models for correcting tropospheric noise.

For Merapi-Merbabu or Merapi areas (Figures 14b and 14c), we observe better performance for GNSS stratified models than weather-based models only for the ascending track. For the descending track, GNSS and ERA5 models show similar performance. At Merapi (8 stations), the proportion of efficient corrections derived from

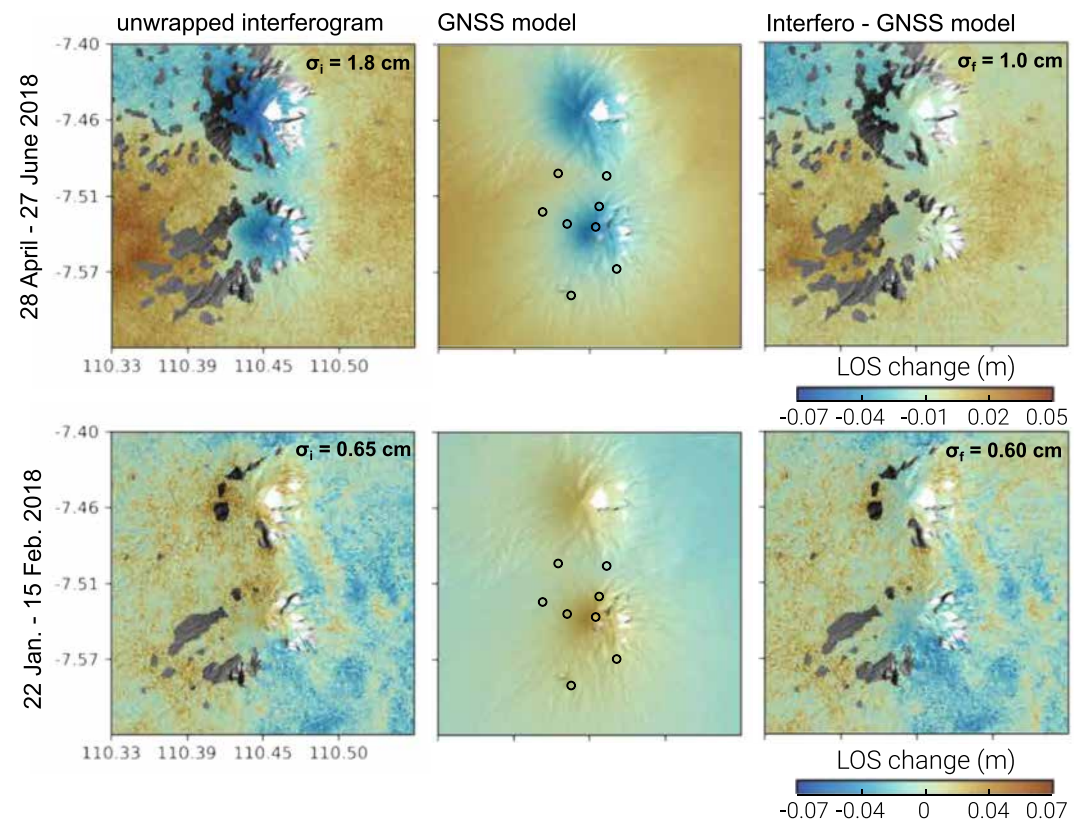


Figure 12. Performance on GNSS models for the two interferograms shown in Figures 6a and 7a. The left panels show the unwrapped interferograms before correction. Middle panels are the models derived from the GNSS stratified delays shown by the circles. The right panels correspond to the corrected interferograms after removing the GNSS models.

GNSS models is $\sim 30\%$ lower than for La Réunion Island (~ 34 stations) for both tracks. It underlines the effect of the number of stations on the performance. Therefore, our proposed strategy for volcanoes having few GNSS stations at different elevations such as Merapi is to use the GNSS stratified models for correcting tropospheric noise as they provide equal (descending) or even better information (ascending) than weather-based models.

6. Discussion: The Importance of Providing Real-Time and Accurate Tropospheric Corrections During InSAR Routine Processing

6.1. Importance of Spatial and Temporal Resolution

In theory, models with the highest temporal and spatial resolution should provide the best tropospheric corrections. However, in practice, there is often a trade-off between the temporal and spatial resolution of the data sets available. Global weather models are spatially interpolated from grids of 10 km (GACOS) and 30 km (ERA5) to the spatial resolution of the interferograms that is a few tens of meters using the information of the DEM. Reanalysis is performed at fixed times from midnight: every 1 hr (ERA5) or every 6 hr (GACOS). As solutions can be shifted from minutes to hours relative to the time of the SAR acquisitions, temporal interpolation is needed in addition to spatial interpolation. In comparison, GNSS models provide the highest temporal resolution (e.g., 5 min for Merapi), but its spatial resolution will depend on the distribution of the stations.

For the two case studies, ERA5 models show better performance than GACOS models for correcting tropospheric signals. Such behavior has been observed in other settings such as the Telica volcano in Nicaragua (Stephens et al., 2020) or a few cities in China (Shihezi, Wuhan and Changchun) (Zhang et al., 2022). Although more comparative studies have to be carried out to better understand in which conditions ERA5 and GACOS models perform best, this result could indicate that the spatial resolution of the models is not the first limiting factor.

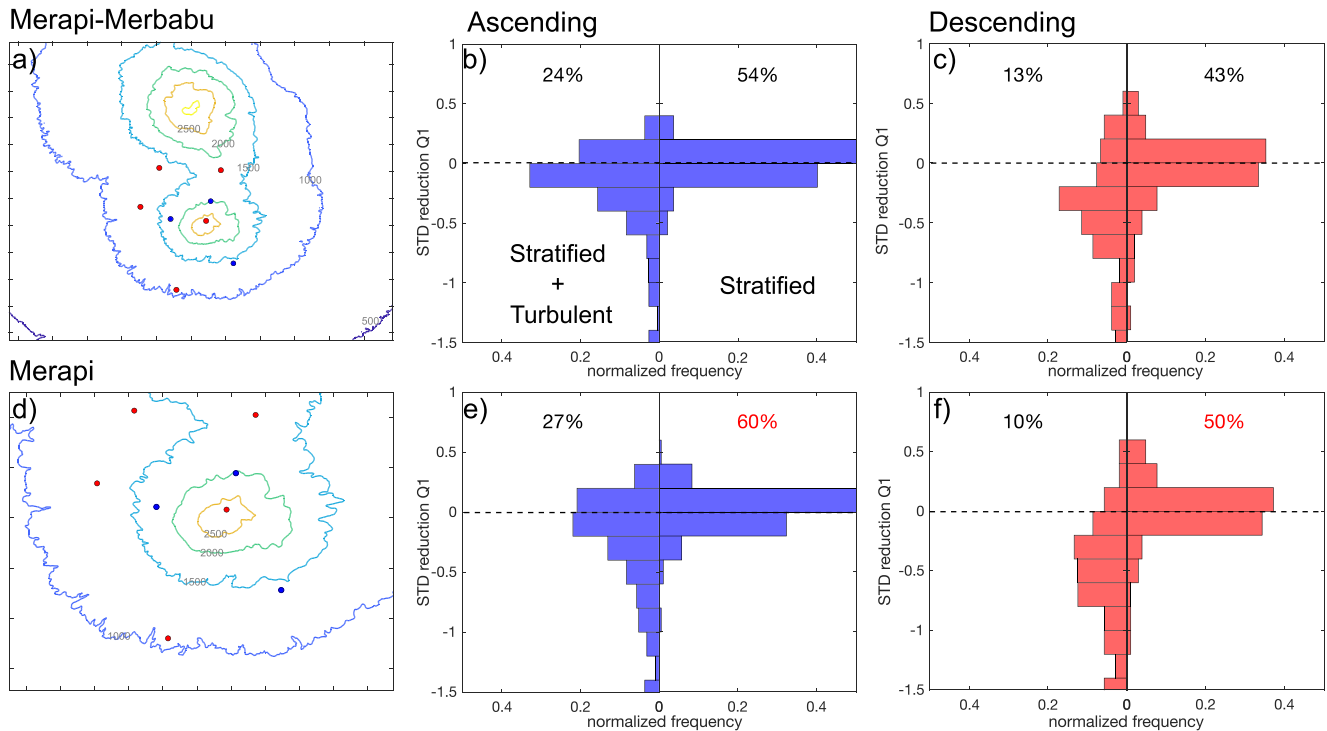


Figure 13. Performance of the GNSS models for correcting tropospheric noise for two areas: (a)–(c) Merapi-Merbabu and (d)–(f) Merapi. We consider the two GNSS networks: DOMERAPI (5 stations - red dots) and SATREPS (3 stations - blue dots). The reduction of the standard deviation (Q1) is calculated for (b)–(e) the ascending (blue) and (c)–(f) the descending (red) data sets. For each panel, the left side corresponds to the GNSS models considering both stratified and turbulent components whereas the right panel corresponds to the GNSS stratified model.

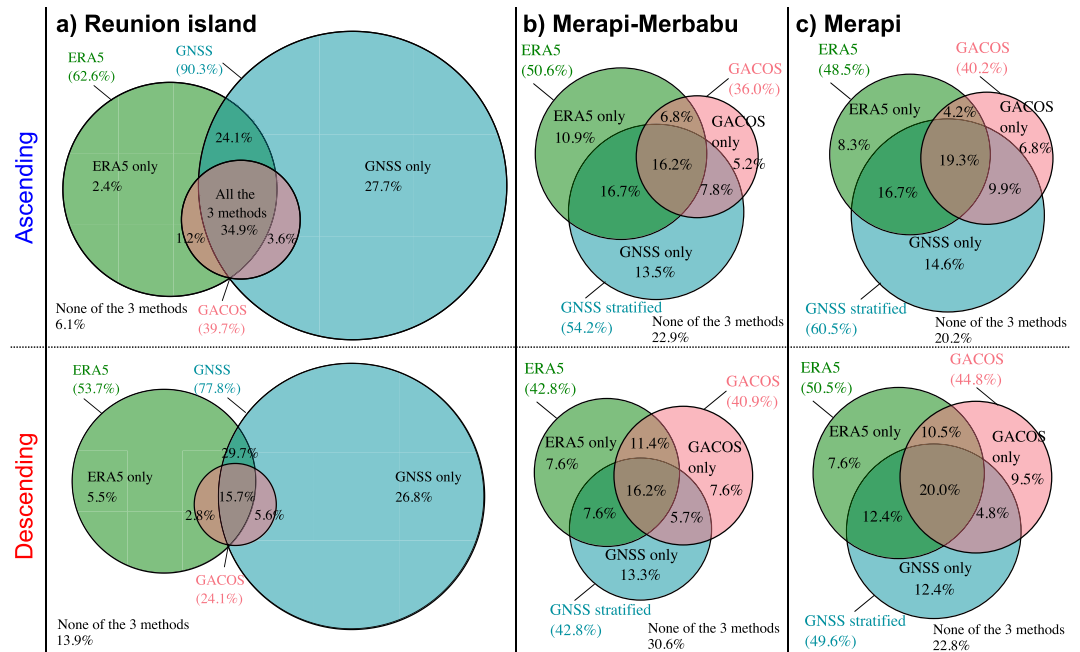


Figure 14. Venn diagram showing the performance of ERA5 model (green), GACOS model (red) and GNSS model (blue) for correcting tropospheric noise for different areas: (a) La Réunion Island, (b) Merapi-Merbabu and (c) Merapi. The size of each circle corresponds to the proportion of interferograms with $Q1 > 0$. The values in the intersection between circles indicate the proportion of interferograms that are corrected by more than one method.

Table 3

Comparison of the Performance of Tropospheric Corrections Using GNSS Models Derived From 5 to 8 Stations for the Two Areas: Merapi-Merbabu (MM) and Merapi (M)

Track Area Criterion	Ascending		Ascending		Descending		Descending	
	MM	MM	M	M	MM	MM	M	M
	$Q1 > 0$	$Q2 > 0$	$Q1 > 0$	$Q2 > 0$	$Q1 > 0$	$Q2 > 0$	$Q1 > 0$	$Q2 > 0$
5 stations	56.8%	58.8%	60.4	64.1%	46.6%	64.7%	53.3%	66.7%
8 stations	54.2%	56.8%	60.4	63.0%	42.8%	58.1%	49.5%	63.8%

Note. Values correspond to the proportion of interferograms with a reduction of the standard deviation ($Q1 > 0$) and the reduction of the phase-elevation correlation ($Q2 > 0$).

Indeed, for the two tropical volcanoes studied, we were able to provide reliable tropospheric delay models derived from a network of GNSS stations located at an average distance of 6–8 km from each other (Table 1). In our cases, tropospheric signals are dominated by the wavelengths of the volcano's topography (e.g., ~10 km for Merapi) or the local perturbations observed on oceanic islands (e.g., ~20–40 km at La Réunion). Therefore, low spatial resolution will only limit our ability to correct turbulent components at scales smaller than a few kilometres.

In terms of time scales, the computation of the average hourly ZTD solutions of the station REUN at la Réunion Island indicates a non-linear trend, especially between 0 and 12 hr UTC (Figure S5b in Supporting Information S1). It is not surprising that tropospheric delays show non-linear behavior on tropical volcanoes. As a result, the linear interpolation performed is likely to over or under-estimate the ZTD measurements depending on the time of the SAR acquisition and the effect will increase with low temporal resolution models. This could explain why ERA5 models are statistically more efficient than GACOS models on both test sites. For future studies, a potential improvement would be to use the information obtained from the GNSS ZTD time series to define non-linear functions for the temporal interpolation of weather models.

In the absence of GNSS local stations, we would recommend using weather models with the highest temporal resolution for correcting tropospheric signals on volcanoes. In cases of well-instrumented volcanoes such as Piton de la Fournaise, Kilauea and Etna, we highly recommend using Zenith Tropospheric Delays derived from the GNSS measurements. Indeed, this approach outperforms the current global weather models for correcting tropospheric noise and more importantly it can be performed with no time latency compared to weather-based models. In cases of volcanic areas instrumented with a limited number of GNSS stations, such as Merapi, results will depend on the number and the spatial distribution of the GNSS stations and therefore, we always recommend first carrying out a statistical analysis to compare the performance between global weather-based models and GNSS locals models. Then, if there is a gain (even low) from GNSS models, it could be relevant to implement the approach during InSAR routine processing as it provides real-time corrected time series of surface displacements that will be suitable for monitoring applications.

6.2. Limitations of the GNSS Approach

As we stated above, the quality of the GNSS model will depend at first order on the number of stations and their spatial distribution over the studied area (both horizontally in x, y and vertically in z). We expect the performance to increase with the number of stations. Indeed, we found an increase in overall performance of ~30% between Merapi (8 stations) and Piton de la Fournaise (~34 stations).

However, the instrumentation of Piton de la Fournaise is exceptional and far from what is currently achievable for most of the active volcanoes. Depending on the context, it is important to quantify the minimum number of GNSS stations required to reach at least similar performance to ERA5 weather-based models and to quantify the benefit of adding a few stations.

To look at the influence of the network, we perform again the statistical analysis on the Merapi volcano by only considering the 5 stations of the DOMERAPI network (Figures S6–S7 in Supporting Information S1). Table 3 shows the comparison of the performance for the criteria $Q1$ and $Q2$ between 5 and 8 stations. We should expect a decrease in the performance with 5 stations. However, results are better with 5 stations than 8 stations. It underlines that adding a few stations will not always induce an increase in the overall performance of the GNSS

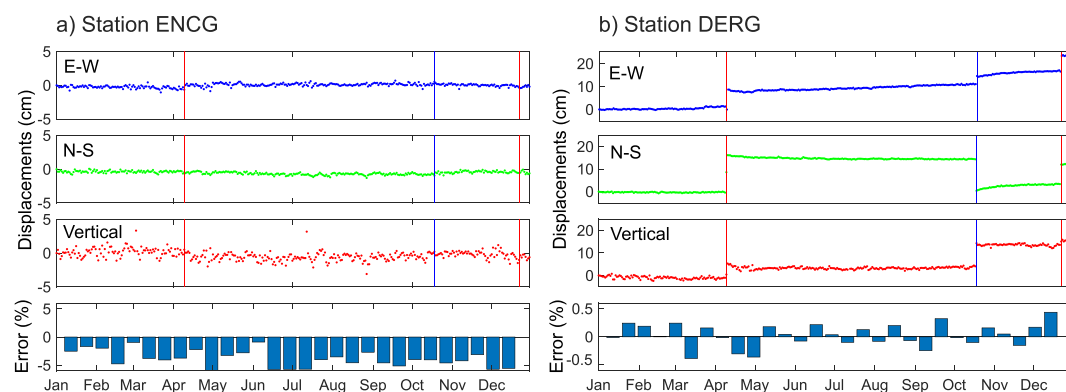


Figure 15. Three top rows correspond to GNSS daily solutions for E-W, N-S and vertical displacements for two stations at Piton de la Fournaise: ENCG (western rim of Enclos Fouqué) and DERG (eastern rim of Dolomieu crater). Vertical lines indicate the three intrusive events (red = eruption; blue = failed eruption). The bottom row shows the errors in the ZTD retrieval based on the cross-validation method for each station.

stratified model. In this context, the SATREPS network does not seem to significantly improve the GNSS stratified model. Furthermore, Table 3 shows that the correction is always better in the Merapi area than in the Merapi-Merbabu area, which is directly linked to the fact that all the GNSS stations are located on the flanks of Merapi. Indeed, the effectiveness of the GNSS network for atmospheric corrections should always be addressed as a function of the area of interest for the specific study under consideration.

6.3. Influence on Ground Displacements on the Retrieval of Tropospheric Delays

During the GNSS processing, the Zenith Tropospheric Delays are derived assuming fixed daily positions for the station. Therefore, we can wonder if rapid ground displacement signals (a few tens of cm) related to dyke intrusions have an effect on the quality of the hourly ZTD solutions retrieved. During the year 2021, three dyke intrusions emplaced in Piton de la Fournaise on 09 April, 18 October and 22 December. Both April and December dyke injections were followed by an eruption whereas the October one did not reach the surface. Distal GNSS stations such as ENCG did not record any displacements (Figure 15a) whereas GNSS stations located close to the dyke intrusions such as DERG recorded steps of a few centimeters in the time series of the three components (Figure 15b).

The performance of the Iterative Tropospheric Decomposition strategy can be tested by using a cross-validation method in which ZTD values retrieved by the ITD model are compared to the ZTD raw values at each station. Figure 15 (bottom rows) shows the relative errors between raw and retrieved values for the two stations: (a) for ENCG station, ITD retrieved values always overestimate raw values with an average error of about -3.9% and (b) for DERG station, ITD retrieved values underestimate or overestimate raw values depending on the epoch with absolute errors remaining lower than 0.5% . We do not observe significant changes in the amplitude of the errors at the timing of the dyke events compared to the baseline period, which demonstrates that short-duration ground displacements do not affect the quality of the retrieval of tropospheric delays. Therefore, our method can be applied to correcting tropospheric artifacts during unrest periods.

6.4. Benefit of GNSS Tropospheric Corrections to Reduce Temporal Noise in InSAR Time Series

The main objective for correcting accurately the tropospheric noise is to increase the signal-to-noise ratio in time series. This will help the characterization of the displacement field by improving the detection of the signal and eventually reducing the uncertainties in the source models. Here, we quantify the reduction of the noise level in the time series after tropospheric corrections for both test sites.

During the period of survey (January 2016–June 2018), the Merapi volcano was at rest with no surface displacements recorded by ground stations. Therefore, the InSAR time series should record the level of noise in the data. For both ascending and descending tracks, InSAR raw velocity maps show a positive signal at the edifice's summit that could indicate a motion toward the satellite (Figures 16a–16d). Mean velocities calculated between

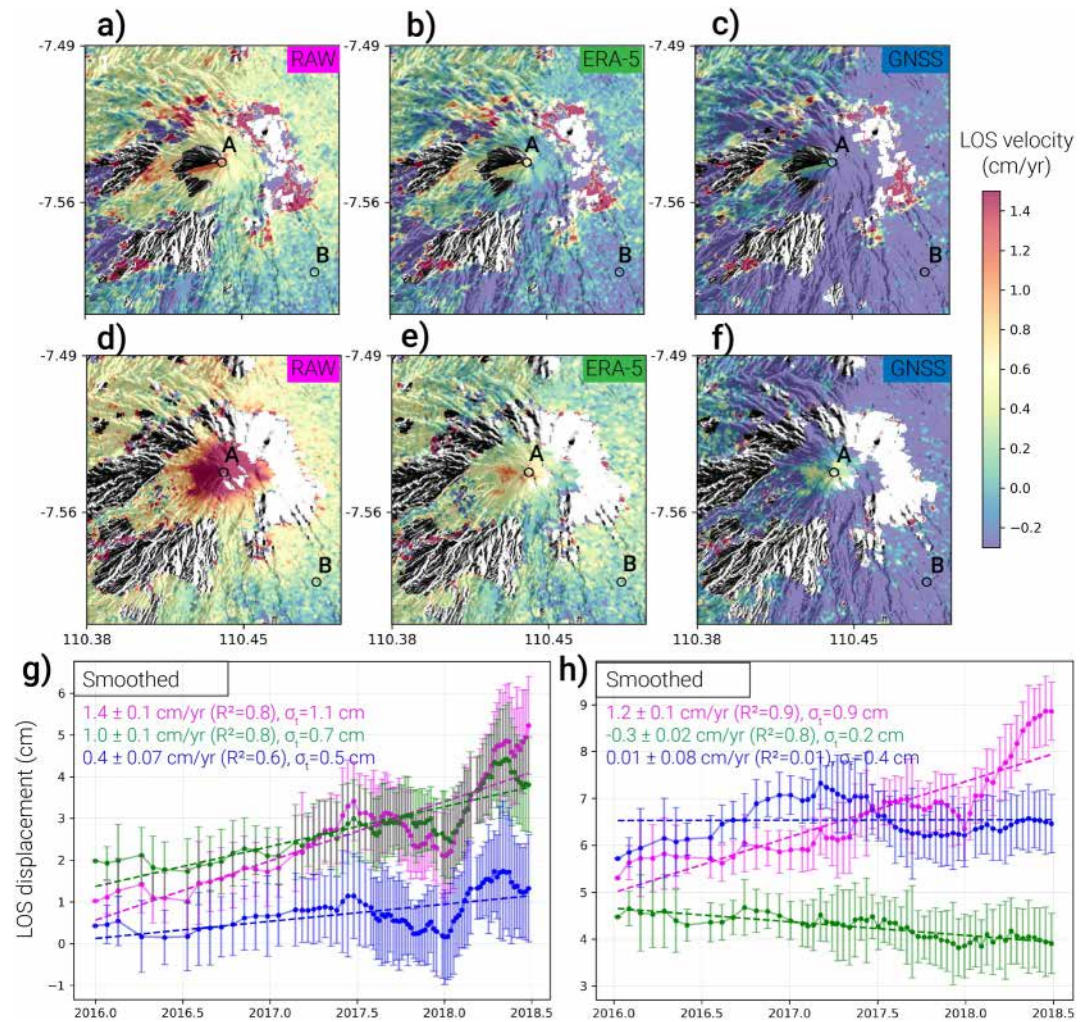


Figure 16. Impact of tropospheric corrections on the quality of InSAR time series at Merapi volcano. (a–f) LOS velocity maps deduced for the raw time series and the corrected series (ERA5 weather-based models and GNSS models) for (a–c) the ascending and (d–f) the descending track; (g), (h) Ascending and descending InSAR time series of the point A considering the point B as the reference (see location in velocity maps) for the raw data set (magenta solid line) and the corrected data set using ERA5 weather-based models (green solid line) and GNSS models (blue solid line). To reduce scatter and identify trends, time series are smoothed over a sliding window of 18 days. Vertical error bars on each data point correspond to the standard deviation calculated on a 5×5 window centered on the pixel location.

the summit (point A) and the base of the volcano (point B) are estimated at 1.4 ± 0.1 and 1.2 ± 0.1 cm/yr for ascending and descending tracks, respectively (Figures 16g and 16h - pink line). For both tracks, we observe a large increase in the displacement rates between January and June 2018. However, the amplitude of the positive signal is largely reduced after performing tropospheric corrections (Figures 16b, 16c, 16e and 16f), which indicates that the signal initially detected is dominated by tropospheric phase delays.

After ERA5 corrections, the mean LOS velocity is reduced to 1.0 ± 0.1 and -0.3 ± 0.02 cm/yr for ascending and descending time series, respectively (Figures 16g and 16h - green line). After GNSS corrections, the mean LOS velocity decreases to 0.4 ± 0.07 and 0.01 ± 0.08 cm/yr for ascending and descending time series, respectively (Figures 16g and 16h - blue line). For both corrections, the reduction of tropospheric signals is more effective for the descending track than for the ascending track.

After GNSS-based corrections, the temporal noise (σ_t) for a 2.5-year time series is reduced by half from 0.9–1.1 to 0.4–0.5 cm. Then, we can expect to detect displacement rates >1 cm/yr at 95% confidence. For the descending track, the reduction of temporal noise is better after ERA5 corrections (0.2 cm) in comparison with GNSS-based

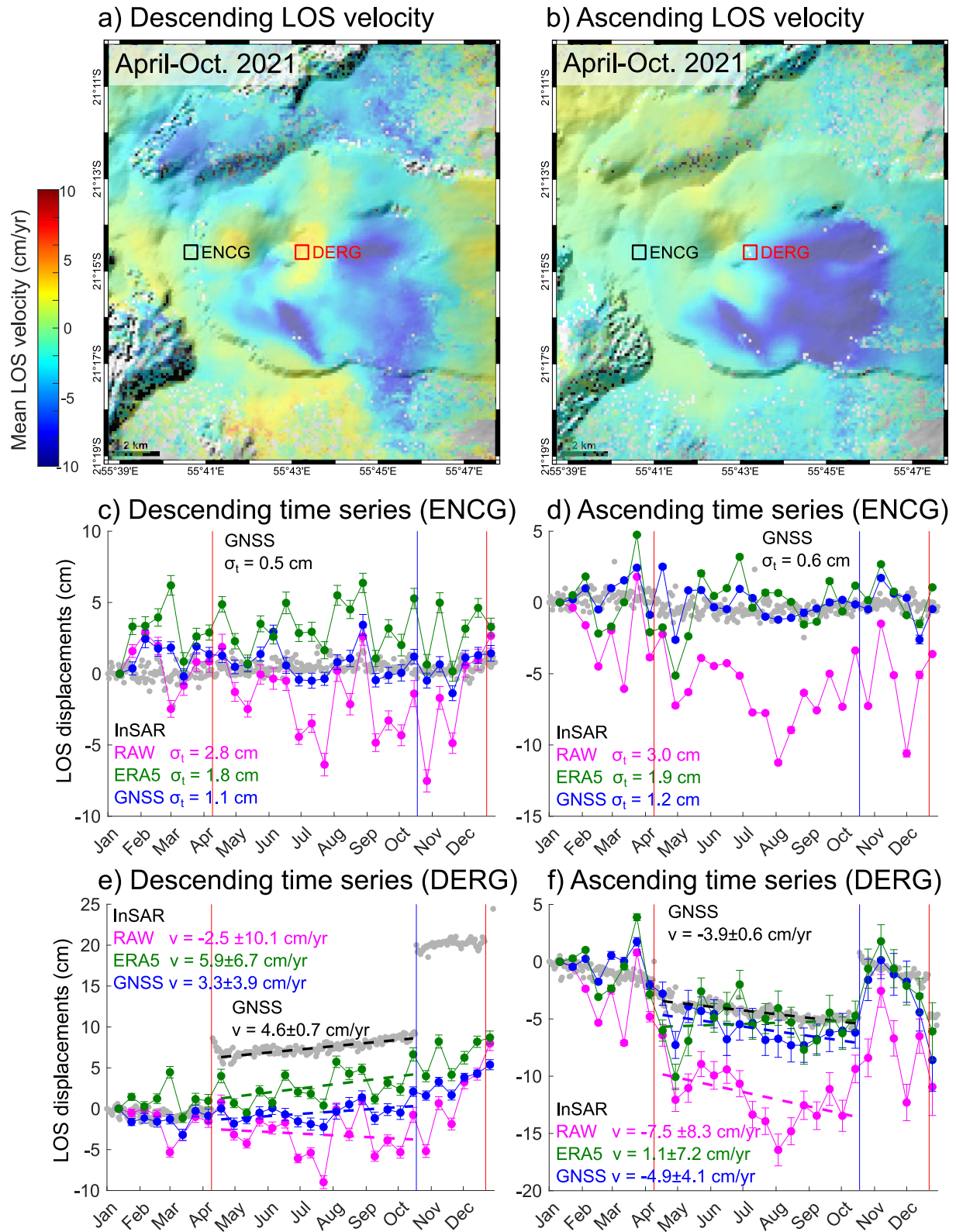


Figure 17.

corrections (0.4 cm). This could be explained by the fact that the ERA5 models correct part of the turbulent noise that is not taken into account in the GNSS approach due to the lack of stations. However, we can observe that the ERA5 corrected time series shows a linear trend of -0.3 cm/yr when we should expect no displacement, suggesting that ERA5 is over-correcting the positive stratified signals. Here, we show that both methods have limitations that depend first order on the characteristics of the noise (turbulent vs. stratified) present on interferograms.

Because ground deformation signals localized at the summit of stratovolcanoes can be the result of the rapid pressurization of the shallow magmatic system leading to an eruption (Biggs et al., 2010; Morales Rivera et al., 2017; Poland, 2024), it is crucial to provide a rapid and accurate analysis of InSAR observations to Volcano Observatories during a period of crisis. Here, we show that the use of routine tropospheric corrections based on real-time GNSS models contributes to this objective by improving the identification and mitigation of tropospheric signals at the Merapi volcano.

At Piton de la Fournaise, the period of the survey is marked by three magma intrusions emplaced successively on 9 April, 18 October, and 22 December 2021. The GNSS station ENCG is located on the western rim of the Enclos Fouqué far from the deformation signals and therefore it did not record any deformation during the year 2021 (see location in Figures 17a and 17b). It will be used as a baseline to estimate the noise level. To compare GNSS and InSAR time series, the GNSS data set (E-W, N-S, Up/Down) were projected into the corresponding Line-Of-Sight (Figures 17c–17f - gray dots). Without atmospheric corrections, both descending and ascending InSAR time series at the ENCG station are largely scattered with a temporal standard deviation σ_t of 2.8 and 3.0 cm, respectively (Figures 17c and 17d - magenta dots) that is five times larger than the noise level recorded for the GNSS time series ($\sigma_t = 0.5$ –0.6 cm). After applying ERA5 corrections, the temporal standard deviation of the InSAR descending and ascending time series is reduced to 1.8 and 1.9 cm (Figures 17c and 17d - green dots). With GNSS-based corrections, the reduction is larger than for ERA5, with a temporal standard deviation of 1.1 and 1.2 cm for descending and ascending time series. These solutions are in good agreement with the GNSS time series. Here, we see the benefit of performing systematic GNSS-based corrections, as it reduces the noise level in a 1-year time series to ~ 1 cm, which is only twice as large as the GNSS noise level.

The GNSS station DERG is located close to the Dolomieu crater (see location in Figures 17a and 17b) and recorded different trends of displacements due to the magmatic activity. GNSS time series show large step-like displacements: (a) ~ 8 and ~ 10 cm of LOS displacements in the descending geometry related to the April and October intrusions (Figure 17e - gray dots) and (b) ~ 6 and ~ 4 cm of LOS displacements in the ascending geometry for the October and December intrusions (Figure 17f - gray dots). For the descending geometry, none of the InSAR time series shows step-like displacements due to the loss of coherence in the area that made the phase unwrapping of the deformation signal quite challenging. For the ascending geometry, it is not easy to identify the step-like displacements in the raw InSAR time series due to the high level of noise (Figure 17f - magenta dots). However, the identification of the step-like displacements is possible using the corrected InSAR time series (Figure 17f - green and blue dots).

In addition to step-like displacements, the GNSS time series showed a linear trend between April and October 2021 with LOS mean velocities (v) of 4.6 ± 0.7 and -3.9 ± 0.6 cm/yr for ascending and descending geometries, respectively (Figures 17e and 17f). Such long-term inter-eruptive signals of a few cm/yr have been detected in GNSS time series during past events and they have been interpreted as the pressurization of magmatic reservoirs ranging from 3.9 to 1.2–1.7 km below the surface (Peltier et al., 2016; Staudacher & Peltier, 2015). So far, these inter-eruptive signals have never been detected in previous InSAR studies. For the raw InSAR time series, the

Figure 17. Impact of tropospheric corrections on the quality of InSAR time series at Piton de la Fournaise. (a), (b) Descending and ascending LOS velocities calculated between April and October 2021, after applying GNSS-based tropospheric corrections. The location of the GNSS stations, ENCG and DERG, are shown by black and red squares. (c), (d) Descending and ascending time series for the year 2021 at the station ENCG. (e), (f) Descending and ascending time series for the year 2021 at the station DERG. Gray dots correspond to the GNSS time series projected into the corresponding line-of-sight. Color dots correspond to the different InSAR time series: raw (magenta), with ERA5 corrections (green) and with GNSS-based corrections (blue). For each data point, the values and error bars are the mean and the standard deviation of the LOS displacements evaluated on a 5×5 window centered on the GNSS location. Vertical solid lines indicate the timing of the three intrusive events (red = eruption; blue = failed eruption). In panels c and d, the temporal standard deviation (σ_t) is indicated for each data set as a proxy for noise level. In panels e and f, the inter-intrusive displacements between 9 April and 18 October are fitted by a linear trend for each time series (dashed lines). Values of v correspond to the LOS velocities and its uncertainties (1σ).

mean velocity values obtained are far from those deduced from the GNSS time series, and the uncertainties are greater than 8 cm/yr. After ERA5 corrections, the time series are less scattered, and therefore, the trends get closer to the GNSS time series; however, the confidence is low as the uncertainties on mean velocities remain around 7 cm/yr. After applying GNSS-based corrections, mean velocity estimates are 3.3 ± 3.9 and -4.9 ± 4.1 cm/yr, which are on the same order of magnitude as the values found for the GNSS data set. Once corrected from the GNSS-based approach, maps for the ascending and descending mean velocities show complex patterns for the inter-intrusive period spanning between April and October 2021 (Figures 17a and 17b). We observe that the small amplitude and localized signal on the crater Dolomieu is largely perturbed by other strong signals: i) a NW-SE elongated negative signal in the south related to the emplacement of the April intrusion ii) a large negative pattern on the eastern flank (with amplitude up to -10 cm/yr in the ascending geometry) previously identified as an area where flank motion is activated by the emplacement of successive intrusions (Dumont et al., 2022). Here, we show that accurate corrections of tropospheric signals based on a dense GNSS network contribute to reducing the signal-to-noise ratio in InSAR time series, allowing for better detection and characterization of both co-eruptive and inter-eruptive signals at Piton de la Fournaise.

7. Conclusions

In response to the occurrence of natural hazards such as volcanic eruptions, it is crucial to design and implement automated systems that can monitor and detect surface displacements in real time. Open-access policy for Sentinel-1 radar images provides large opportunities for the scientific community to develop such automated InSAR processing systems. Although InSAR products can be available a few hours after the SAR acquisition, access to weather-based atmospheric corrections remains a limitation for near real-time applications as the products are available a few days after the present. Our statistical analysis based on two tropical volcanoes, Piton de la Fournaise and Merapi, shows that the performance of the corrections remains low for GACOS models with a reduction of the tropospheric noise for only 24%–45% of the data sets and average for ERA5 models with a reduction of the tropospheric noise for 43%–63% of the data sets. Our analysis of these two test sites indicates that ERA5 corrections perform better than GACOS corrections, which underlines that the temporal resolution of the model is first-order more important than the spatial resolution. Compared to weather-based models, GNSS ZTD measurements are available in near real-time on Volcano Observatories and GNSS map delays only require a few minutes to be produced. In addition, the standard processing of GNSS data provides tropospheric delays at high temporal resolution ranging from 5 min to 1 hr. For Piton de la Fournaise, by using ~ 34 stations, GNSS models reduce the tropospheric noise for 80%–90% of the data sets, which corresponds to an increase of the performance of $\sim 25\%$ in comparison with ERA5 models. As expected, the performance is lower for Merapi than for Piton de la Fournaise as the former volcano is less instrumented. However, our results show that with 5 stations, GNSS models already reach the performance obtained with ERA5 models. Therefore, our approach can be applied to a large number of active volcanoes as long as they have few GNSS stations distributed at different elevations. The production of corrected InSAR time series using GNSS tropospheric models can support the routine monitoring of ground displacements on active volcanoes and improve the detection of volcanic unrest. For the two test sites, the GNSS-based corrections decrease the noise level in the InSAR time series by a factor of two in comparison with the raw time series. At Piton de la Fournaise, the corrected InSAR time series enables the retrieval of inter-eruptive displacements. Between April and October 2021, the rate of displacements is found to be ~ 3.3 cm/yr for the descending time series and ~ -4.9 cm/yr for the ascending InSAR time series, which are in good agreement with the amplitude derived from GNSS time series (4.6 and -3.9 cm/yr).

Data Availability Statement

InSAR products have been processed with the LiCSAR automated system (Lazecký et al., 2020) for la Réunion island and with NSBAS processing chain (Doin et al., 2011) for Merapi volcano. InSAR data sets and weather-based models are available in a Zenodo repository (Albino et al., 2024). GNSS data sets for La Réunion Island are available via the Volobsis portal (Beauducel et al., 2024). The python package "MANGO" (Mitigating Atmospheric noise using GNSS Observations) used to produce the GNSS-based tropospheric corrections is available in Gitlab repository (<https://gricad-gitlab.univ-grenoble-alpes.fr/albinof/mango.git>).

Acknowledgments

This work has been supported by the Programme National de Télédétection Spatiale (PNTS, Grant PNTS-2022-06), the CNES project MagmaTrack, the Instrumented Site VELI (IRD) and the Laboratoire Mixte International SIR (IRD). We thank the Associate Editor, Shin-Chan Han, and two anonymous reviewers who provided valuable comments, which improved the scientific impact of the study.

References

- Albino, F., Biggs, J., Yu, C., & Li, Z. (2020). Automated methods for detecting volcanic deformation using sentinel-1 InSAR time series illustrated by the 2017–2018 unrest at Agung, Indonesia. *Journal of Geophysical Research: Solid Earth*, 125(2), e2019JB017908. <https://doi.org/10.1029/2019jb017908>
- Albino, F., Gremion, S., & Pinel, V. (2024). Sentinel-1 interferograms and weather-based tropospheric delays maps (ERA5, GACOS) for two volcanoes: Piton de la Fournaise and Merapi. *Zenodo*. [Dataset]. <https://doi.org/10.5281/zenodo.13471043>
- Beauducel, F., Boissier, P., Briole, P., Charade, O., Peltier, A., Sakic, P., et al. (2024). Zenith Tropospheric Delays at La Reunion island for the year 2021 derived from the processing of GNSS stations. *IPGP Research Collection*. [Dataset]. <https://doi.org/10.18715/IPGP.2024.lswuhqhf>
- Beauducel, F., Briole, P., & Froger, J.-L. (2000). Volcano-wide fringes in ERS synthetic aperture radar interferograms of Etna (1992–1998): Deformation or tropospheric effect? *Journal of Geophysical Research*, 105(B7), 16391–16402. <https://doi.org/10.1029/2000jb900095>
- Béjar-Pizarro, M., Socquet, A., Armijo, R., Carrizo, D., Genrich, J., & Simons, M. (2013). Andean structural control on interseismic coupling in the North Chile subduction zone. *Nature Geoscience*, 6(6), 462–467. <https://doi.org/10.1038/ngeo1802>
- Bekaert, D., Hooper, A., & Wright, T. (2015). A spatially variable power law tropospheric correction technique for InSAR data. *Journal of Geophysical Research: Solid Earth*, 120(2), 1345–1356. <https://doi.org/10.1002/2014jb011558>
- Bertiger, W., Bar-Sever, Y., Dorsey, A., Haines, B., Harvey, N., Hemberger, D., et al. (2020). GipsyX/RTGx, a new tool set for space geodetic operations and research. *Advances in Space Research*, 66(3), 469–489. <https://doi.org/10.1016/j.asr.2020.04.015>
- Biggs, J., Mothes, P., Ruiz, M., Amelung, F., Dixon, T. H., Baker, S., & Hong, S.-H. (2010). Stratovolcano growth by co-eruptive intrusion: The 2008 eruption of Tungurahua Ecuador. *Geophysical Research Letters*, 37(21). <https://doi.org/10.1029/2010gl044942>
- Biggs, J., & Pritchard, M. E. (2017). Global volcano monitoring: What does it mean when volcanoes deform? *Elements*, 13(1), 17–22. <https://doi.org/10.2113/gselements.13.1.17>
- Biggs, J., Wright, T., Lu, Z., & Parsons, B. (2007). Multi-interferogram method for measuring interseismic deformation: Denali Fault, Alaska. *Geophysical Journal International*, 170(3), 1165–1179. <https://doi.org/10.1111/j.1365-246x.2007.03415.x>
- Budi-Santoso, A., Beauducel, F., Nandaka, I. G. M. A., Humaida, H., Costa, F., & Widiwijayanti, C. (2023). The Merapi volcano monitoring system. In *Merapi volcano: Geology, eruptive activity, and monitoring of a high-risk volcano* (pp. 409–436). Springer.
- Cao, Y., Jónsson, S., & Li, Z. (2021). Advanced InSAR tropospheric corrections from global atmospheric models that incorporate spatial stochastic properties of the troposphere. *Journal of Geophysical Research: Solid Earth*, 126(5), e2020JB020952. <https://doi.org/10.1029/2020jb020952>
- Cavalié, O., Doin, M.-P., Lasserre, C., & Briole, P. (2007). Ground motion measurement in the Lake Mead area, Nevada, by differential synthetic aperture radar interferometry time series analysis: Probing the lithosphere rheological structure. *Journal of Geophysical Research*, 112(B3). <https://doi.org/10.1029/2006jb004344>
- Costantini, M., Minati, F., Trillo, F., Ferretti, A., Novali, F., & Passera, E. (2021). European ground motion service (EGMS). In *2021 IEEE International Geoscience and Remote Sensing Symposium IGARSS* (pp. 3293–3296).
- de Munck, J., & Spoelstra, T. (1992). Refraction of transatmospheric signals in geodesy. In *Proceedings of the symposium, the Hague, The Netherlands*.
- Doin, M.-P., Guillaso, S., Jolivet, R., Lasserre, C., Lodge, F., Ducret, G., & Grandin, R. (2011). Presentation of the small baseline NSBAS processing chain on a case example: The Etna deformation monitoring from 2003 to 2010 using Envisat data. In *Proceedings of the fringe symposium* (pp. 3434–3437).
- Doin, M.-P., Lasserre, C., Peltzer, G., Cavalié, O., & Doubre, C. (2009). Corrections of stratified tropospheric delays in SAR interferometry: Validation with global atmospheric models. *Journal of Applied Geophysics*, 69(1), 35–50. <https://doi.org/10.1016/j.jappgeo.2009.03.010>
- Dumont, Q., Cayol, V., Froger, J.-L., & Peltier, A. (2022). 22 years of satellite imagery reveal a major destabilization structure at Piton de la Fournaise. *Nature Communications*, 13(1), 2649. <https://doi.org/10.1038/s41467-022-30109-w>
- Ebmeier, S. K., Biggs, J., Mather, T. A., & Amelung, F. (2013). Applicability of InSAR to tropical volcanoes: Insights from Central America. *Geological Society, London, Special Publications*, 380(1), 15–37. <https://doi.org/10.1144/sp380.2>
- Elliott, J. R., Biggs, J., Parsons, B., & Wright, T. (2008). InSAR slip rate determination on the Altyn Tagh Fault, northern Tibet, in the presence of topographically correlated atmospheric delays. *Geophysical Research Letters*, 35(12). <https://doi.org/10.1029/2008gl033659>
- Emardson, T., Simons, M., & Webb, F. (2003). Neutral atmospheric delay in interferometric synthetic aperture radar applications: Statistical description and mitigation. *Journal of Geophysical Research*, 108(B5). <https://doi.org/10.1029/2002jb001781>
- Gertisser, R., Charbonnier, S. J., Keller, J., & Quidelleur, X. (2012). The geological evolution of Merapi volcano, central Java, Indonesia. *Bulletin of Volcanology*, 74(5), 1213–1233. <https://doi.org/10.1007/s00445-012-0591-3>
- Guerova, G., Jones, J., Douša, J., Dick, G., de Haan, S., Pottiaux, E., et al. (2016). Review of the state of the art and future prospects of the ground-based GNSS meteorology in Europe. *Atmospheric Measurement Techniques*, 9(11), 5385–5406. <https://doi.org/10.5194/amt-9-5385-2016>
- Hanssen, R. F. (2001). *Radar interferometry: Data interpretation and error analysis* (Vol. 2). Springer Science and Business Media.
- Herring, T., King, R., & McClusky, S. (2010). *Introduction to gamit/globk*. Massachusetts Institute of Technology.
- Hooper, A., Zebker, H., Segall, P., & Kampes, B. (2004). A new method for measuring deformation on volcanoes and other natural terrains using InSAR persistent scatterers. *Geophysical Research Letters*, 31(23). <https://doi.org/10.1029/2004gl021737>
- Hopfield, H. S. (1971). Tropospheric effect on electromagnetically measured range: Prediction from surface weather data. *Radio Science*, 6(3), 357–367. <https://doi.org/10.1029/rs006i003p00357>
- Jin, S., Luo, O., & Gleason, S. (2009). Characterization of diurnal cycles in ZTD from a decade of global GPS observations. *Journal of Geodesy*, 83(6), 537–545. <https://doi.org/10.1007/s00190-008-0264-3>
- Jolivet, R., Grandin, R., Lasserre, C., Doin, M.-P., & Peltzer, G. (2011). Systematic InSAR tropospheric phase delay corrections from global meteorological reanalysis data. *Geophysical Research Letters*, 38(17). <https://doi.org/10.1029/2011gl048757>
- Jung, J., Kim, D.-j., & Park, S.-E. (2013). Correction of atmospheric phase screen in time series InSAR using WRF model for monitoring volcanic activities. *IEEE Transactions on Geoscience and Remote Sensing*, 52(5), 2678–2689. <https://doi.org/10.1109/tgrs.2013.2264532>
- Lazecký, M., Spaans, K., González, P. J., Maghsoudi, Y., Morishita, Y., Albino, F., et al. (2020). LiCSAR: An automatic InSAR tool for measuring and monitoring tectonic and volcanic activity. *Remote Sensing*, 12(15), 2430. <https://doi.org/10.3390/rs12152430>
- Liang, H., Zhang, L., Ding, X., Lu, Z., & Li, X. (2018). Toward mitigating stratified tropospheric delays in multitemporal InSAR: A quadtree aided joint model. *IEEE Transactions on Geoscience and Remote Sensing*, 57(1), 291–303. <https://doi.org/10.1109/tgrs.2018.2853706>
- Massonet, D., Rossi, M., Carmona, C., Adragna, F., Peltzer, G., Feigl, K., & Rabaute, T. (1993). The displacement field of the Landers earthquake mapped by radar interferometry. *Nature*, 364(6433), 138–142. <https://doi.org/10.1038/364138a0>
- Meyer, F. (2010). A review of ionospheric effects in low-frequency SAR—Signals, correction methods, and performance requirements. In *2010 IEEE International Geoscience and Remote Sensing Symposium* (pp. 29–32).

- Morales Rivera, A. M., Amelung, F., Mothes, P., Hong, S.-H., Nocquet, J.-M., & Jarrin, P. (2017). Ground deformation before the 2015 eruptions of Cotopaxi volcano detected by InSAR. *Geophysical Research Letters*, 44(13), 6607–6615. <https://doi.org/10.1002/2017gl073720>
- Murray, K. D., Bekaert, D. P., & Lohman, R. B. (2019). Tropospheric corrections for InSAR: Statistical assessments and applications to the Central United States and Mexico. *Remote Sensing of Environment*, 232, 111326. <https://doi.org/10.1016/j.rse.2019.111326>
- Murray, K. D., Lohman, R. B., & Bekaert, D. P. (2020). Cluster-based empirical tropospheric corrections applied to InSAR time series analysis. *IEEE Transactions on Geoscience and Remote Sensing*, 59(3), 2204–2212. <https://doi.org/10.1109/tgrs.2020.3003271>
- Onn, F., & Zebker, H. (2006). Correction for interferometric synthetic aperture radar atmospheric phase artifacts using time series of zenith wet delay observations from a GPS network. *Journal of Geophysical Research*, 111(B9). <https://doi.org/10.1029/2005jb004012>
- Parker, A. L., Biggs, J., Walters, R. J., Ebmeier, S. K., Wright, T. J., Teanby, N. A., & Lu, Z. (2015). Systematic assessment of atmospheric uncertainties for InSAR data at volcanic arcs using large-scale atmospheric models: Application to the Cascade volcanoes, United States. *Remote Sensing of Environment*, 170, 102–114. <https://doi.org/10.1016/j.rse.2015.09.003>
- Peltier, A., Bachèlery, P., & Staudacher, T. (2009). Magma transport and storage at Piton de La Fournaise (La Réunion) between 1972 and 2007: A review of geophysical and geochemical data. *Journal of Volcanology and Geothermal Research*, 184(1–2), 93–108.
- Peltier, A., Beauducel, F., Villeneuve, N., Ferrazzini, V., Di Muro, A., Aiuppa, A., et al. (2016). Deep fluid transfer evidenced by surface deformation during the 2014–2015 unrest at Piton de la Fournaise volcano. *Journal of Volcanology and Geothermal Research*, 321, 140–148. <https://doi.org/10.1016/j.jvolgeores.2016.04.031>
- Pinel, V., Hooper, A., De la Cruz-Reyna, S., Reyes-Davila, G., Doin, M., & Bascou, P. (2011). The challenging retrieval of the displacement field from InSAR data for andesitic stratovolcanoes: Case study of Popocatepetl and Colima Volcano, Mexico. *Journal of Volcanology and Geothermal Research*, 200(1–2), 49–61. <https://doi.org/10.1016/j.jvolgeores.2010.12.002>
- Pinel, V., Poland, M. P., & Hooper, A. (2014). Volcanology: Lessons learned from synthetic aperture radar imagery. *Journal of Volcanology and Geothermal Research*, 289, 81–113. <https://doi.org/10.1016/j.jvolgeores.2014.10.010>
- Poland, M. P. (2024). Remote sensing of volcano deformation and surface change. In *Remote sensing for characterization of geohazards and natural resources* (pp. 173–203). Springer.
- Remy, D., Bonvalot, S., Briole, P., & Murakami, M. (2003). Accurate measurements of tropospheric effects in volcanic areas from SAR interferometry data: Application to Sakurajima volcano (Japan). *Earth and Planetary Science Letters*, 213(3–4), 299–310. [https://doi.org/10.1016/s0012-821x\(03\)00331-5](https://doi.org/10.1016/s0012-821x(03)00331-5)
- Rémy, D., Chen, Y., Froger, J.-L., Bonvalot, S., Cordoba, L., & Fustos, J. (2015). Revised interpretation of recent InSAR signals observed at Llaima volcano (Chile). *Geophysical Research Letters*, 42(10), 3870–3879. <https://doi.org/10.1002/2015gl063872>
- Richter, N., & Froger, J.-L. (2020). The role of Interferometric Synthetic Aperture Radar in detecting, mapping, monitoring, and modelling the volcanic activity of Piton de la Fournaise, La Réunion: A review. *Remote Sensing*, 12(6), 1019. <https://doi.org/10.3390/rs12061019>
- Rosen, P. A., Hensley, S., Zebker, H. A., Webb, F. H., & Fielding, E. J. (1996). Surface deformation and coherence measurements of Kilauea Volcano, Hawaii, from SIR-C radar interferometry. *Journal of Geophysical Research*, 101(E10), 23109–23125. <https://doi.org/10.1029/96je01459>
- Rott, H., & Nagler, T. (2006). The contribution of radar interferometry to the assessment of landslide hazards. *Advances in Space Research*, 37(4), 710–719. <https://doi.org/10.1016/j.asr.2005.06.059>
- Saastamoinen, J. (1973). Contributions to the theory of atmospheric refraction: Part II. Refraction corrections in satellite geodesy. *Bulletin Geodesique*, 107(1), 13–34. <https://doi.org/10.1007/bf02522083>
- Schmidt, D. A., & Bürgmann, R. (2003). Time-dependent land uplift and subsidence in the Santa Clara valley, California, from a large interferometric synthetic aperture radar data set. *Journal of Geophysical Research*, 108(B9). <https://doi.org/10.1029/2002jb002267>
- Shamshiri, R., Motagh, M., Nahavandchi, H., Haghighi, M. H., & Hoseini, M. (2020). Improving tropospheric corrections on large-scale Sentinel-1 interferograms using a machine learning approach for integration with GNSS-derived zenith total delay (ZTD). *Remote Sensing of Environment*, 239, 111608. <https://doi.org/10.1016/j.rse.2019.111608>
- Shirzaei, M., & Bürgmann, R. (2012). Topography correlated atmospheric delay correction in radar interferometry using wavelet transforms. *Geophysical Research Letters*, 39(1). <https://doi.org/10.1029/2011gl049971>
- Sparks, R., Biggs, J., & Neuberg, J. (2012). Monitoring volcanoes. *Science*, 335(6074), 1310–1311. <https://doi.org/10.1126/science.1219485>
- Staudacher, T., & Peltier, A. (2015). Ground deformation at Piton de la Fournaise, a review from 20 years of GNSS monitoring. In *Active volcanoes of the southwest indian ocean: Piton de la fournaise and karthala* (pp. 251–269). Springer.
- Stephens, K. J., Wauthier, C., Bussard, R. C., Higgins, M., & LaFemina, P. C. (2020). Assessment of mitigation strategies for tropospheric phase contributions to InSAR time-series datasets over two Nicaraguan volcanoes. *Remote Sensing*, 12(5), 782. <https://doi.org/10.3390/rs12050782>
- Thollard, F., Clesse, D., Doin, M.-P., Donadieu, J., Durand, P., Grandin, R., et al. (2021). Flatsim: The form@ter large-scale multi-temporal sentinel-1 interferometry service. *Remote Sensing*, 13(18), 3734. <https://doi.org/10.3390/rs13183734>
- Wicks Jr, C. W., Dzurlin, D., Ingebritsen, S., Thatcher, W., Lu, Z., & Iverson, J. (2002). Magmatic activity beneath the quiescent Three Sisters volcanic center, central Oregon Cascade Range, USA. *Geophysical Research Letters*, 29(7). <https://doi.org/10.1029/2001gl014205>
- Wright, T., Parsons, B., & Fielding, E. (2001). Measurement of interseismic strain accumulation across the North Anatolian Fault by satellite radar interferometry. *Geophysical Research Letters*, 28(10), 2117–2120. <https://doi.org/10.1029/2000gl012850>
- Yip, S. T. H., Biggs, J., & Albino, F. (2019). Reevaluating volcanic deformation using atmospheric corrections: Implications for the magmatic system of Agung volcano, Indonesia. *Geophysical Research Letters*, 46(23), 13704–13711. <https://doi.org/10.1029/2019gl085233>
- Yu, C., Li, Z., & Penna, N. T. (2018). Interferometric synthetic aperture radar atmospheric correction using a GPS-based iterative tropospheric decomposition model. *Remote Sensing of Environment*, 204, 109–121. <https://doi.org/10.1016/j.rse.2017.10.038>
- Yu, C., Li, Z., Penna, N. T., & Crippa, P. (2018). Generic atmospheric correction model for interferometric synthetic aperture radar observations. *Journal of Geophysical Research: Solid Earth*, 123(10), 9202–9222. <https://doi.org/10.1029/2017jb015305>
- Yu, C., Penna, N. T., & Li, Z. (2017). Generation of real-time mode high-resolution water vapor fields from GPS observations. *Journal of Geophysical Research: Atmospheres*, 122(3), 2008–2025. <https://doi.org/10.1002/2016jd025753>
- Zebker, H. A., Rosen, P. A., & Hensley, S. (1997). Atmospheric effects in interferometric synthetic aperture radar surface deformation and topographic maps. *Journal of Geophysical Research: Solid Earth*, 102(B4), 7547–7563. <https://doi.org/10.1029/96jb03804>
- Zhang, Z., Lou, Y., Zhang, W., Wang, H., Zhou, Y., & Bai, J. (2022). Assessment of ERA-Interim and ERA5 reanalysis data on atmospheric corrections for InSAR. *International Journal of Applied Earth Observation and Geoinformation*, 111, 102822. <https://doi.org/10.1016/j.jag.2022.102822>